Large-scale Signal Propagation Modes in the Human Brain

Youngjo Song[1*], Pyeong Soo Kim[2], Benjamin A. Philip[3], Taewon Kim[4,5*]

[1]MORESCIENCE, Seoul, Republic of Korea

[2]Department of Brain & Cognitive Sciences,

College of Life Science and Bioengineering,

Korea Advanced Institute of Science and Technology (KAIST),

Daejeon, Republic of Korea

[3]Program in Occupational Therapy,

Washington University School of Medicine, St. Louis, MO

[4]Department of Physical Medicine and Rehabilitation,

Penn State College of Medicine, Hershey, PA

[5]Department of Kinesiology,

Penn State University, University Park, PA

*** Address correspondence to:**

Youngjo Song, Ph.D.

Email: ys1j13@gmail.com

MORESCIENCE, 95, Banpo-daero 24-gil, Seocho-gu, Seoul, South Korea; Tel: +82-2-525-4254.

Taewon Kim, Ph.D.

Email: tbk5452@psu.edu

90 Hope Drive, Suite 2105, Hershey, PA 17033; Tel: +1-979-422-9014.

Abstract

The dynamic allocation of neural resources throughout brain-wide networks is essential for optimal brain operation. However, the neural principles underlying the facilitation of such allocation remain inadequately understood. In this work, we address this gap by uncovering brain-wide coherent causal structures in resting-state fMRI timeseries data. We identified five distinct and interpretable modes of signal propagation that most effectively predict future blood-oxygen-level-dependent (BOLD) signals. Each identified mode uniquely represents specific aspects of neural resource allocation among established networks: (1) signal propagation along cortical hierarchy; (2) the salience network's modulation between default mode and the central executive networks; (3) the mapping between visual and sensorimotor areas with frontal modulation; and (4) interhemispheric interaction. Notably, four of these modes were associated with the default mode network, highlighting its central role as a functional hub. Collectively, these modes account for a broad spectrum of well-known dynamical properties in the brain. Importantly, individual variability in these modes correlates with general cognitive abilities, is influenced by genetic factors, and exhibits stability across different cognitive tasks. Together, these modes not only integrate previously disparate phenomena observed in fMRI data but also offer a concise framework for characterizing individual functional fingerprints within BOLD signals.

Article

A fundamental aspect of brain function is its ability to dynamically allocate neural resources across large-scale, distributed networks, integrating and coordinating information processing [1-4]. Recent advancements in the study of brain dynamics have yielded significant insights into the neural mechanisms that underpin this capability. For example, signal propagation along the cortical hierarchy—bidirectionally between unimodal regions, such as primary sensory and motor areas, and transmodal regions that overlap with the default mode network (DMN) [5-7]—in both human and macaque monkey brains illustrates the coherent neural resource allocation across this axis [8-10]. This coherent allocation exemplifies the systematic management and coordination of neural resources. This dynamic interaction encompasses both bottom-up processes, such as sensory integration, and top-down mechanisms, such as the modulation of unimodal processing by transmodal regions, all of which are essential for facilitating high-level cognitive functions [7, 11-14].

Building upon such coherent allocation of neural resources, the DMN functions as a central hub for facilitating the relay and integration of abstract information processed along the cortical hierarchy [12, 15] through its interactions with various large-scale networks [16, 17]. In response to task-related demands, the brain dynamically reallocates neural resources between distinct functional networks. Specifically, neural resources shift from the task-negative (TN) network—i.e., DMN, which is activated during internally focused and self-referential processes—to the task-positive (TP) network, which includes the central executive network (CEN) activated during goal-directed tasks [1, 18-20]. Robust spatiotemporal patterns identified in resting-state fMRI data suggest that fundamental causal structures underlie the anticorrelation between TN and TP networks (i.e., coherent decrease of BOLD activities in TN regions with coherent increase in TP regions), even in the absence of explicit tasks [21-23]. These findings suggest that the brain maintains an intrinsic organization that facilitates efficient

transitions between internally and externally focused states.

Analyses of task-related dynamics reveal that the salience network (SN), which responds to behaviorally relevant stimuli [24], modulates this brain-wide anticorrelation by regulating the engagement and disengagement of TN and TP networks [25-27]. Changes in this modulatory mechanism serve as vital indicators of cognitive performance variations. For instance, the relationships between the DMN and CEN networks shift in response to cognitive demands [22], and alterations—such as insufficient suppression of the DMN during task performance—are correlated with reduced attention and poorer task outcomes [28, 29]. Furthermore, disruptions in these network interactions have been associated with a range of neurological and psychiatric disorders [1, 30], emphasizing the necessity of understanding the mechanisms that regulate neural resource allocation. Thus, elucidating how the brain orchestrates activity across extensive networks can provide deeper insights into the neural basis of cognition. However, no comprehensive physiological and phenomenological theoretical framework yet exists to integrate the extensive findings related to the brain's dynamic structures.

Leveraging brain-wide coherence in causal dynamics offers a promising strategy for addressing this complex challenge. In this context, dynamic mode decomposition (DMD) is identified as a powerful, equation-free, data-driven technique that effectively captures the coherent dynamics exhibited by high-dimensional systems [31]. DMD operates by solving eigenvector problems based on a linear approximation of the causal dynamics that govern signal flow within the system ($\boldsymbol{x}(t) = A\boldsymbol{x}(t-1)$). This approach decomposes multi-dimensional time-series data into a set of temporally coherent and spatially distributed modes, referred to as dynamic modes (DM). (It is important to note that DM will be used exclusively to indicate dynamic mode, while DMN will refer specifically to the default mode network.). The application of DMD facilitates explicit and parsimonious modeling of the spatially distributed temporal dynamics present in high-dimensional datasets. This methodology allows

for understanding the system-wide causal structure, facilitating assessments of how patterns evolve and interact over time, evaluations of system stability, and predictions of future states [32-36].

In this study, we aimed to elucidate the large-scale causal structures underlying neural resource allocation in the brain by systematically employing DMD on whole-brain fMRI time-series data. This framework enabled the identification of five distinct modes of signal propagation within the brain, which not only predict future BOLD signals but also account for major dynamics observed in resting-state fMRI. These dynamics encompass the topography of functional connectivity (FC) and its temporal fluctuations, known as time-varying FC (TVFC); FC-based functional gradients [5, 37]; wave-like signal propagation along cortical hierarchies [8-10]; global signals [38]; time-lag structures [39]; quasi-periodic patterns (QPP) [21, 22]; the anticorrelation between TN and TP networks [23]; and hemispheric lateralization observed in resting-state BOLD dynamics [40]. Moreover, the DMs identified in this study correspond to critical dimensions of neural resource allocation among established large-scale networks. By elucidating these modes, we aim to provide a novel and parsimonious framework that integrates the brain's dynamic structures, thereby enhancing our understanding of neural resource allocation and its impact on cognitive function.

Results

To model the temporal dynamics of the global BOLD signal, we applied DMD to resting-state fMRI scans from the Human Connectome Project (HCP) Young Adult S1200 dataset. We utilized the Glasser parcellation [41] to subdivide the cortical regions into 360 parcels and the Cole-Anticevic Brain-wide network partition [42] to divide the subcortical and cerebellar regions into 356 parcels, resulting in a total of 716 regions of interest (ROIs) (see Methods).

Subsequently, we utilized a forward-backward DMD algorithm [43] to compute the DMs of the group-level causal connectivity matrix (i.e., matrix A), which best approximates the evolution of the BOLD signal between adjacent time points across all subjects (see Methods section "Group-level DMD" for details). To ensure physiological relevance, we retained only DMs with oscillation frequencies within the range of 0.01 Hz to 0.1 Hz, consistent with the filter frequency used in the fMRI preprocessing step.

To determine the optimal number of DMs for accurately describing brain-wide BOLD signal dynamics, we utilized a 5-fold cross-validation approach, evaluating predictive performance for future BOLD signals across varying numbers of DMs. In each fold, the training set was used to estimate the DMs (using the group-level DMD). Each resting-state fMRI run in the test set was further divided into test-fitting and test-validation data. The test-fitting data were used to estimate the DM metrics—parameters that determine how signals sustain their influence and how quickly they propagate within each DM—enabling prediction of the brain-wide signal at subsequent time points. We estimated these DM metrics by projecting the brain-wide BOLD signal onto the DMs and then optimizing to minimize the prediction error ($\boldsymbol{\varepsilon}(t) = \boldsymbol{x}(t) - \hat{\boldsymbol{x}}(t|t-1)$), where $\boldsymbol{x}(t)$ is the BOLD signal at time t and $\hat{\boldsymbol{x}}(t|t-1)$ is the predicted BOLD signal at time t based on prior information up to $t-1$ (for details see subsequent results and Methods section "Subject-level estimation of DM metrics"). For model comparison, we utilized the cross-validated R^2 measure, which quantifies the proportion of variance in the signal that the model can explain based on the prediction error within the test-validation segment (see Methods section "Optimizing the number of DMs"). The methodology for DMD and DM metric estimation is illustrated in Figure 1a.

Remarkably, the results of DMD (i.e., DMs) remained highly consistent across all five cross-validation folds (Supplementary Result 1), with each fold identifying twelve DMs, demonstrating the robustness of our DMD approach. Cross-validation results indicated that

five DMs were optimal to predict the temporal evolution of BOLD signal (Figure 1b). Notably, even when using a single DM, we achieved a lower prediction error (i.e., higher cross-validated R^2) compared to the linear and non-linear models, which had previously demonstrated the best performance in previous evaluations [44].

The reconstructed cortical FC matrix using these five DMs showed a strong correlation with the original group-FC matrix (R = 0.83; Figure 1c). Network community analysis revealed a strong correspondence between the community structures of the original and reconstructed FC networks, with a normalized mutual information (NMI) value of 0.62—indicating that 87.5% of nodes are matched, and reflecting high similarity in community organization. Furthermore, the TVFC, summarized by standard deviation (std), also showed a strong correlation between the original and reconstructed TVFC matrices (R = 0.75; Supplementary Figure 3a), suggesting that temporal fluctuations of FC are captured by the temporal evolution of the five DMs. These findings collectively suggest that the five DMs parsimoniously encapsulate the essential dynamics and organizational features of brain-wide BOLD signal activity, effectively reconstructing both the static and dynamic aspects of FC. Importantly, these five DMs correspond to temporal transitions between well-recognized brain-wide networks, which will be elaborated in subsequent sections.

[Figure 1]

DM1: Principal DM accounts for signal propagation along the cortical hierarchy

The temporal dynamics of a linear system are predominantly governed by the DM with the largest eigenvalue [45]. In our analysis of resting-state fMRI data, the DM with the highest eigenvalue—referred to as the "principal DM"—demonstrated signal propagation between unimodal regions (i.e., primary visual, secondary visual, primary SM, and primary auditory

areas) and the transmodal areas (largely overlapping with the DMN) (Figure 2a). Importantly, in our cross-validation analyses aimed at predicting future BOLD signals (Figure 1b), the principal DM was consistently included, whether employing a single DM model or incorporating various configurations of DMs. Consistent with its designation as the DM possessing the largest eigenvalue, the utilization of solely the principal DM resulted in superior predictive performance when compared to both linear and non-linear models. Moreover, this principal DM accounted for the majority of variance explained across all predictions, irrespective of the number of DMs used.

The observed signal propagation between unimodal and transmodal areas is supported by the correlation between the spatial activity patterns of the principal DM at each reconstructed time point and the principal FC gradient. This correlation achieved a peak negative correlation of –0.83 during activation of unimodal regions and a peak positive correlation of 0.83 during activation of transmodal regions (see the inset of Figure 2a). The principal FC gradient is well-recognized for its alignment with the cortical hierarchy defined both anatomically and functionally [5]. Thus, these findings suggest that the majority of the brain-wide coherent dynamics are driven by information exchange along the cortical hierarchy (i.e., unimodal-transmodal axis), aligning with the wave propagation along cortical hierarchy [8-10]. Supplementary Video 1 depicts the signal propagation within the principal DM.

Building on the principal DM's prominent eigenvalue, we hypothesized that the principal DM predominantly governs the key characteristics of resting-state dynamics. Consistent with this hypothesis, the cosine values of phase differences between ROIs—an exact reconstruction of FC between phase-locked ROIs—within the principal DM were moderately correlated with the cortical FC matrix ($R = 0.42$; Figure 2b). Furthermore, the std of temporal fluctuations in FC, as observed in the fMRI signal, was also moderately correlated with the predicted std calculated using only the phase differences in the principal DM ($R = 0.39$; Figure 2F). These

findings suggest that the global FC distribution and its fluctuations are significantly influenced by signal propagation along the cortical hierarchy.

To further elucidate this relationship, we examined the association between the time-lag structure and the ROI's phase differences within this DM. Time lag refers to the delay or causal dependence between two brain signals, where one signal is temporally delayed relative to another, thereby representing the overall temporal precedence or lag of each ROI (around ± 2 seconds) [39]. Similarly, the phase difference between ROIs quantifies the extent to which one ROI's activation is temporally delayed relative to another within this DM. We observed a strong correlation between the lag projection—the average time delay (i.e., time-lag) between ROIs—calculated with fMRI signal and the average phase delay in the principal DM ($R = 0.72$; Figure 2c), supporting the major contribution to the brain's overall dynamics. Additionally, the time-series of the principal DM achieved a peak correlation with QPP [21, 46]—a time-lag phenomenon occurring at longer timescales (~20 seconds)—of $R = 0.93$ (Figure 2d). This high correlation is noteworthy, given that time-lag structures and QPP are phase-delayed phenomena occurring at different timescales, suggesting that both arise from the brain-wide signal propagation captured by the principal DM. Furthermore, the global signal was predominantly correlated with the global activity of the fMRI signal projected onto the principal DM (mean $R = 0.63$, the highest among the five DMs; see Supplementary Figure 5), underscoring the principal DM's dominant contribution to the global signal.

Extending beyond cortical regions, the principal functional gradients of subcortical areas—including the hippocampus, striatum, thalamus, brain stem, and amygdala—and the cerebellum also exhibited strong alignment with the principal DM, each achieving peak correlations exceeding $R > 0.7$ (see Supplementary Figure 8). These functional gradients capture the dominant variations in functional organization within subcortical and cerebellar FC. Therefore, this observation further highlights the critical role of the principal DM in signal propagation

along the dominant functional variations, not only within cortical regions but also robustly across subcortical structures and the cerebellum. Overall, these results establish the principal DM as a key unifying factor in explaining various brain network behaviors.

[Figure 2]

DM2&3: Dynamic shift between the three major large-scale networks (DMN, CEN, and SN)

In our analysis, we identified two distinct DMs associated with interactions and transitions among the DMN, CEN, and SN—three major intrinsic large-scale brain networks. These DMs exhibited unique transition pathways contingent upon SN activation (Figure 3). Specifically, one mode involved a transition from the SN to the DMN, accompanied by suppression of the CEN, which we term the "SN-to-DMN" DM (Figure 3a). Conversely, the other mode involved a transition from the SN to the CEN, also accompanied by suppression of the DMN, was referred to as the "SN-to-CEN" DM (Figure 3b). This contrasting dissociation of the DMs highlights the SN's role as a dynamic switching hub capable of modulating the activity of the DMN and CEN by either facilitating or suppressing them. These findings align with recent perspectives that position the SN as a causal signaling hub responsible for network switching between the DMN and CEN [25, 26, 30, 47, 48].

Notably, in each DM, the transition from the SN to either the DMN or the CEN was followed by subsequent activation in the previously suppressed network. For instance, in the SN-to-DMN DM, the initial activation of the SN led to increased activity in the DMN and suppression of the CEN, which was eventually followed by reactivation of the CEN. Conversely, in the SN-to-CEN DM, activation of the SN led to increased activity in the CEN and suppression of the DMN, followed by reactivation of the DMN. This was evidenced by the correlation between the spatial patterns at each reconstructed time point of these DMs and

either the DMN (or TN network: PCC-seed based functional connectivity network; see Supplementary Figure 9a) or CEN (derived from Yeo's 7-network parcellation and considered as the TP network) (Figure 3a, b). These results emphasize the inherent anticorrelation between the TN and TP networks [23, 49].

To further assess the reflection of this anti-correlation in the identified DMs, we compared them to the well-established spatiotemporal patterns of TN and TP network anti-correlation, specifically the anti-correlated QPP obtained after global signal regression (GSR) [21]. The anti-correlated QPP exhibited only moderate correlations with these DMs (SN-to-DMN: R = 0.54; SN-to-CEN: R = 0.41). However, when the principal DM was incorporated to reconstruct the time series, the correlations with the anti-correlated QPP increased significantly (SN-to-DMN: R = 0.80; SN-to-CEN: R = 0.59) (see Figure 3c). This enhancement suggests that the anti-correlated QPP emerges from the combination of two distinct transitions: one from the DMN to unimodal regions (represented by the principal DM) and the other from the DMN to the CEN (represented by the SN-to-DMN DM).

Our findings indicate that GSR does not eliminate the influence of the principal DM, even though it reduces it significantly. The global signal—which reflects widespread fluctuations in brain activity—correlates more strongly with the reconstructed signals that include both the principal DM and the SN-to-DMN DM (mean R = 0.79) than with signals reconstructed using only the principal DM (mean R = 0.63; see previous section). Furthermore, the global signal showed the second-highest correlation with the global activity of the fMRI signal projected onto the SN-to-DMN DM (Supplementary Figure 5). This suggests that the principal DM remains a dominant contributor to the global signal, while the SN-to-DMN DM acts as a sub-dominant factor that further influences the global signal.

[Figure 3]

DM4: Frontovisual-to-sensorimotor propagation in the brain

Our analysis further identified a distinct DM characterized by a pattern in which activity from the frontal and visual (FV) regions synchronizes and transitions into sensorimotor (SM) regions (referred to as "FV-to-SM" DM; Figure 4a), which are essential for processing sensory information and executing motor functions. We evaluated the correlation between the spatial patterns at each reconstructed time point of this DM and the second FC gradient (see Supplementary Figure 4b topography of the second FC gradients), which delineates functional variation along the visual-SM axis of the brain [5]. The correlation with the second FC gradient exhibited significant peaks, reaching a negative peak of -0.85 and a positive peak of 0.85. These results indicate signal propagation within this DM along the visual-SM axis, potentially reflecting the flow of information from sensory input to motor output. Regarding this, the synchronized activity between frontal regions and visual areas underscores the critical role of frontal regions in orchestrating the interaction between motor outputs and sensory inputs [50, 51].

DM5: Bilaterally asymmetric DM

Among the five DMs, the final DM exhibited bilateral asymmetry in its spatiotemporal pattern, highlighting the significance of hemispheric lateralization in the resting-state brain dynamics. This bilaterally asymmetric DM (bi-asym DM) initiates activation in the visual regions, subsequently progresses to the left DMN regions. The activation then transitions to transmodal regions that exhibit a robust correlation with the principal FC gradient (R = 0.81) and largely overlap with the DMN. It then shifts to the right DMN and visual regions (Figure 4b). The correlation between the spatial pattern at each reconstructed time point and the spatial topography of laterality index (LI)—which indicates whether a ROI exhibits greater

synchronization with the left or right hemisphere (see Methods)—reaches peaks of -0.91 and +0.91. This finding suggests that the bi-asym DM captures significant elements of hemispheric lateralization in resting-state brain dynamics, as quantified by the LI. Moreover, the periodic oscillations observed between the left and right hemispheres in this DM indicate an intrinsic dynamic structure that facilitates continuous interhemispheric communication.

[Figure 4]

Characterizing brain-wide signal propagation via DM metrics: genetic influences and behavioral associations

In summary, the five DMs provide a parsimonious yet comprehensive framework for describing resting-state fMRI dynamics. Each DM is associated with specific operational functions: signal propagation along the unimodal-transmodal axis; dynamic TN/TP network switching of the SN; mapping from visual to SM regions with frontal modulation; and hemispheric lateralization in brain dynamics. Leveraging these DMs, we investigate their potential as a foundational framework for characterizing brain operations. By projecting the brain-wide fMRI signals onto the low-dimensional manifold defined by the five DMs, we effectively distill the complex spatiotemporal distributions of brain activity into their most operationally relevant components.

This dynamic projection is summarized using three distinct subject-specific metrics for each DM: (1) mode-engagement level, (2) persistence rate, and (3) progression rate. The mode-engagement level ($\bar{b}_k$) is obtained by projecting all brain-wide BOLD signals onto the DM space, reflecting the average strength (i.e., average engagement) of each DM during the fMRI scan. The persistence and progression rates (r_k and θ_k) are derived by modeling the causal

dynamics as the temporal evolution of the five DMs, characterized by subject-specific evolution coefficients ($d_k = r_k e^{i\theta_k}$). The persistence rate is given by the magnitude of the evolution coefficients, indicating how strongly a DM is sustained at the next time point. The progression rate is given by the argument (phase) of the evolution coefficients, representing the rate (i.e., speed) at which the associated neural activity patterns evolve within each mode (for mathematical details see "Group-level DMD"). Consequently, each DM yields one mode-engagement level, one persistence rate, and one progression rate, resulting in a total of 15 metrics (collectively referred to as "DM metrics") that describe subject-specific brain-wide BOLD dynamics. The subject-averaged DM metric values are illustrated in Supplementary Figure 11a.

To assess the biological relevance and cognitive significance of these DM metrics, we examined their heritability and association with cognitive traits and behaviors. First, we investigated the genetic underpinnings of the DM metrics using twin analyses that incorporate kinship information. Heritability was estimated using the ACE model [52], which decomposes variance into additive genetic (A), common environmental (C), and unique environmental (E) components. Our results revealed significant genetic contributions to the mode-engagement levels of the five DMs ($h^2 = 0.52$, 95% CI: [0.42, 0.60], $p = 0.0018$), their persistence rates ($h^2 = 0.26$, 95% CI: [0.17, 0.34], $p = 0.0008$) and their progression rates ($h^2 = 0.36$, 95% CI: [0.24, 0.48], $p = 0.0002$). Further supporting these findings, we calculated the cosine distance between each pair of monozygotic (MZ) twins, dizygotic (DZ) twins, siblings, and unrelated individuals (Figure 5a). For mode-engagement levels, persistence rates, and progression rates, the five DMs exhibited greater similarity (i.e., lower cosine distance) among MZ twins compared to DZ twins ($p = 8.23 \times 10^{-4}$, $p = 0.002$, and $p = 0.001$, respectively). Additionally, DZ twins and siblings showed greater similarity than unrelated individuals (DZ vs unrelated: $p = 6.13 \times 10^{-5}$, $p = 0.0086$ and $p = 0.0012$, respectively; siblings vs unrelated: $p = 2.66 \times 10^{-9}$,

$p = 1.05 \times 10^{-6}$ and $p = 3.56 \times 10^{-12}$, respectively). No significant differences were observed between DZ twins and siblings ($p = 0.11$, $p = 0.60$ and $p = 0.72$, respectively).

Next, to explore the cognitive significance of the DM metrics, we examined their correlations with participants' cognitive traits and behaviors. We utilized previously established latent factors derived from behavioral items in the HCP dataset [53]: (1) mental health, (2) cognition, (3) processing speed, and (4) substance use. Correlation analyses were conducted between these four behavioral factors and the DM metrics, controlling for age, sex, handedness, and the cube root of intracranial volume (ICV) and total gray-matter volume (TGMV) as confounding variables (Figure 5b). We found that the cognition factor, reflecting intellectual abilities across various domains, was positively correlated with the mode-engagement level of the SN-to-DMN DM ($t = 3.69$, $p = 0.0148$, FWE-corrected) and negatively correlated with the mode-engagement level of the FV-to-SM DM ($t = -3.51$, $p = 0.0285$, FWE-corrected). Similarly, the processing speed factor, reflecting efficiency of cognitive processing, was positively correlated with the mode-engagement level of the SN-to-CEN DM ($t = 3.42$, $p = 0.0382$, FWE-corrected) and negatively correlated with the mode-engagement level of the principal DM ($t = -3.39$, $p = 0.0434$, FWE-corrected). These results indicate that a higher presence of the SN-to-DMN and SN-to-CEN DMs in BOLD dynamics is associated with better behavioral performance, emphasizing the significance of these DMs in task performance.

The persistence and progression rates also showed correlations with the cognition and processing speed factors. Specifically, the persistence rate of the SN-to-CEN DM was positively correlated with the cognition factor ($t = 3.77$, $p < 0.0117$, FWE-corrected), further indicating the significance of this DM in task performance. The progression rate of the bi-asym DM was positively correlated with both the cognition factor ($t = 4.94$, $p < 1 \times 10^{-4}$, FWE-corrected) and processing speed ($t = 3.39$, $p = 0.0432$, FWE-corrected), supporting the notion that lateralized dynamics are related to cognitive abilities. These results underscore that

dynamic features–such as the degree to which the involvement of DMs is sustained (as indicated by the persistence rate) and the speed at which they evolve (as indicated by the progression rate)–are also related to cognitive abilities. Detailed statistical results for the behavioral analyses are provided in Supplementary Tables 1-6. Overall, the dynamical characteristics represented by the DM metrics reflect important latent factors associated with general cognitive performance.

Individual signatures of DMs are largely preserved during tasks

We further investigated whether the overall signatures of DMs remain consistent during task performance. To test this, we analyzed task-state fMRI data from the HCP dataset, which includes seven distinct tasks: emotional processing, gambling, language comprehension, motor execution, relational reasoning, social cognition, and working memory (N-back) tasks [54]. Each task engages different basic cognitive aspects, providing a comprehensive assessment of brain dynamics under varying cognitive demands.

Our analysis confirmed that all five DMs were significantly present during every task ($p < 1 \times 10^{-100}$; see Methods), underscoring the robust presence of these core dynamic structures across different task conditions. Furthermore, we observed that the relative patterns of both magnitude and phase for the five DMs closely matched those seen during the resting state. Specifically, the cosine similarity (CS) values exceeded 0.98 for mode-engagement levels, greater than 0.999 for persistence rates, and over 0.75 for progression rates when comparing task states to rest (Figure 5c). These high CS values demonstrate a remarkable similarity between resting-state and task-state DMs, supporting the notion that the brain's intrinsic dynamic architecture is preserved during task execution [55]. Therefore, these results indicate that the overall signatures of DMs are stable features of brain activity that persist even as cognitive demands change.

Moreover, we found that the CS values for DM metrics within the same subject across different tasks were all significantly higher than the CS values between different subjects performing the same task. For the mode-engagement levels, the average CS between different tasks for the same subject was 0.989, which was significantly higher (i.e., more similar) than the average CS between different subjects performing the same task (average CS = 0.991; paired t-test, 95% CI for difference = [-0.002, -0.0019] $p = 2.01 \times 10^{-218}$). Similarly, the persistence and progression rates for the same subject between different tasks were significantly more similar (persistence rate: average CS = 0.999716; progression rate: average CS = 0.747) than those for the same task between different subjects (persistence rate: average CS = 0.999684, paired t-test, 95% CI for difference = [-3.60×10^{-05}, -2.79×10^{-05}], $p = 1.95 \times 10^{-53}$; progression rate: average CS =0.728, paired t-test, 95% CI for difference = [-0.021, -0.015], $p = 2.91 \times 10^{-28}$). In sum, individual differences in DMs are consistent across different tasks, highlighting the stability of individual DM signatures.

While the overall signatures of DMs are preserved during tasks, we also observed task-dependent changes in the magnitude and phase of specific DMs. Specifically, the mode-engagement level of the principal DM was significantly reduced during task execution compared to the resting state; in contrast, the SN-to-DMN, SN-to-CEN, and FV-to-SM DMs exhibited increased engagement (Figure 5d), highlighting their enhanced involvement in task-related processes. The progression rates of the SN-to-DMN and SN-to-CEN DMs increased during all seven tasks compared to rest, while other DMs mostly decreased (Figure 5e), implicating changes in the anti-correlation between TP and TN networks during tasks.

Furthermore, we detected significant variations in DMs between different tasks, suggesting that specific cognitive demands can modulate brain dynamics. For instance, the principal DM was significantly more engaged during social tasks, which involve interpreting social interactions (Figure 5f). This increased engagement may reflect the necessity for integrating

information across widespread brain regions to comprehend complex social cues. Conversely, the principal DM exhibited greater persistence during N-back tasks, which require heightened working memory and sustained attention (Supplementary Figure 13). This increased persistence may indicate the need for maintaining stable neural representations over time to support working memory processes. Additional differences are provided in Supplementary Figures 12–14. These findings indicate that while the core dynamic modes are maintained, their relative contributions vary depending on the nature of the task, highlighting the flexibility of the brain's dynamic architecture in adapting to specific cognitive demands.

[Figure 5]

Discussion

Here, we identified five large-scale signal propagation modes (i.e., DMs) that establish a parsimonious schema of the causal dynamics in the brain. These modes effectively predict future BOLD signals and capture various well-established dynamical properties of the brain. Furthermore, the identified modes closely correspond with the dynamic transitions among recognized large-scale brain networks, suggesting they reflect the brain's dynamic allocation of neural resources. By projecting brain-wide signals onto these five DMs, we derived compact dimensions that characterize individual differences in brain dynamics. These differences were associated with domain-general cognitive abilities, were influenced by genetic factors, and remained consistent across various tasks, emphasizing their operational relevance.

Our identification of the five distinct DMs elucidates critical operational aspects of brain function, each corresponding to fundamental neural processes. The principal DM (DM1) captures the dominant signal propagation within the brain, reflecting the intrinsic flow of

information between unimodal sensory regions and transmodal association areas [8-10]. This observation likely signifies multisensory integration in transmodal regions and top-down modulation to unimodal areas. Furthermore, this finding is consistent with earlier descriptions of transitions between extrinsic and intrinsic systems as two temporal "metastates" [56] and aligns with the first principal component identified in prior applications of complex PCA to fMRI datasets [57]. These converging lines of evidence highlight the principal DM's significant role in brain dynamics, as revealed by various spatiotemporal pattern detection methodologies. The robust association between DM1 and key spatiotemporal structures—such as the principal functional gradient encompassing the cortex, subcortical areas, and cerebellum [5, 37]; wave propagation patterns [8-10]; transitions between metastates [56]; global signal [38]; lag structure [39]; and QPP [21]—further highlights the dominance of this signal propagation. Additionally, these associations suggest that the propagation characterized by the principal DM serves as a common source for these diverse spatiotemporal phenomena. The persistence of this dominant mode during task performance indicates its potential involvement in goal-directed cognitive functions.

A notable finding of our study is the identification of propagation modes reflecting the dynamic interplay among the three major large-scale networks namely, the DMN, CEN, and SN—captured in DM2 and DM3 (SN-to-DMN and SN-to-CEN DMs). The activation of the SN can lead to engagement of either the DMN or the CEN, potentially modulating transitions between internally focused and externally oriented cognitive states. This finding underscores the SN's role as a pivotal switching hub between the DMN and CEN, as proposed in the well-established triple-network model [26, 30]. Furthermore, the involvement of the DMN and CEN was followed by activation of the opposing network, indicating the well-known anticorrelation between TN and TP networks (i.e., DMN and CEN) [23, 29]. The relative dominance of these DMs positively correlated with domain-general cognitive abilities (Figure 5b), aligning with

previous reports associating strong anticorrelation of TN/TP networks with flexible task-related resource allocation [58, 59]. This suggests that signal propagation between these networks is crucial for task-related processes, and that modulation by the SN plays a significant role.

The FV-to-SM DM (DM4) represents the synchronization and propagation of activity from frontal and visual regions to SM areas. This associated with the second cortical FC gradient, which varies along the visual-SM axis [5], thereby highlighting the integration of sensory inputs with motor outputs essential for coordinated action. The observed synchronization between frontal and visual regions suggests that modulation within frontal regions plays a critical role in this integration.

Finally, the bi-asym DM (DM5) reveals bilaterally asymmetric dynamics, emphasizing the significance of hemispheric lateralization in cognitive processing and inter-hemispheric communication. The propagation within this DM strongly reflects the LI, demonstrating that this single method (i.e., DMD) can also capture the prominent lateralized spatiotemporal patterns previously identified through more sophisticated methodologies [40]. Signal propagation within this DM oscillates between the left and right hemispheres, indicating a pattern of interhemispheric communication. The, observed propagation speed (as indicated by the progression rate), suggests facilitation of interhemispheric communication, which is considered a crucial factor for high-level cognitive functions (e.g., working memory) and processing speed [60-62]. Consistent with this, the propagation speed of this DM was associated with higher cognitive performance and processing speed (Figure 5b), thereby suggesting that enhanced interhemispheric communication is linked to superior cognitive abilities. It is noteworthy that only this DM is unique in exhibiting a behavioral association with propagation speed. Furthermore, the involvement of the visual network and the DMN during the interhemispheric transitions may signify their critical roles in this communication process, highlighting the necessity for further investigation in future studies.

Notably, the overall signatures of the DMs (represented by DM metrics) are genetically influenced and largely preserved across different task conditions. The DM metrics are more similar within subjects across tasks than between subjects on the same task, underscoring stable aspects of the brain's functional topology [55]. However, we also observed task-dependent modulations in DMs, characterized by increased involvement and facilitation in the SN-to-DMN and SN-to-CEN DMs, alongside a relative decrease in the principal and FV-to-SM DMs. This aligns with the operational interpretation of the SN-to-DMN and SN-to-CEN DMs as being involved in task-related processing, potentially capturing the task-modulation of anticorrelation of TN/TP networks [22, 63]. Overall, these findings enhance our understanding of how the brain maintains core functional dynamics while adapting to varying cognitive demands.

Among the five DMs, four (the principal DM, SN-to-DMN DM, SN-to-CEN DM, and bi-asym DM) are associated with the DMN. This widespread association underscores the DMN's pivotal role as a central functional hub in the brain, responsible for integrating and coordinating diverse types of information across various neural regions [20]. However, we noted minor differences in DMN activation among these DMs. For instance, the ventromedial prefrontal cortex (VMPFC) is rather deactivated during DMN-like activation in the principal DM (Figure 2a), but it is activated during DMN-like activation in the SN-to-DMN and SN-to-CEN DMs (Figure 3a, b). Further differences were observed in the ventrolateral PFC and temporal regions during DMN-like activation in these DMs. These variations may reflect operational distinctions among DMN nodes: for example, the VMPFC might be more relate to task-related processing [64-66]. This could explain the division of subnetworks within the DMN [67-69], warranting further exploration in future studies.

Our framework also offers an interpretation for global signals in the brain, a topic of extensive discussion in the neuroimaging field [38, 70-73]. Our observations indicate that the

major contributor to the global signal is the propagation along the unimodal-transmodal axis, as indicated by the principal DM, but it is also significantly influenced by the anticorrelation between task-negative and task-positive networks in the SN-to-DMN DM. Consequently, GSR significantly reduces the predominant propagation along the unimodal-transmodal axis from the original fMRI time series, making subsequent analyses more sensitive to other signal propagations in the brain [71]. However, our findings suggest that GSR does not entirely remove the influence of the principal DM, as evidenced by the significant explanatory ability of the principal DM in anticorrelated QPPs even after GSR. Therefore, our observations offer new insights into the ongoing debates surrounding the interpretation of global signals and the use of GSR in neuroimaging.

It is important to note that the five DMs we focused on are not exhaustive patterns of signal propagation in the brain. Although additional DMs identified in the group-level dynamic mode decomposition do not enhance the predictive ability for future BOLD signals, these modes may be potential candidates for nuisance aspects of brain dynamics, which should be addressed in future studies. Moreover, one limitation of projecting onto DMs is that the estimation of DM metrics depends on the presence of other DMs during projection due to the non-orthogonality of DM vectors. Therefore, characterizing the residual projections associated with additional DMs is essential for accurately capturing an individual's brain dynamics within this DM framework.

In conclusion, we have proposed five fundamental brain-wide signal propagation modes in the human brain that effectively capture the dominant dynamical characteristics of brain function and exhibit distinct associations with crucial operational and cognitive aspects. This framework provides unified insights into various dynamic characteristics of the brain. Furthermore, the DM-based framework for describing brain dynamics demonstrates a streamlined approach for characterizing individual neural fingerprints, suggesting its potential

application in representing alterations in patients' brain dynamics.

Methods

HCP dataset and preprocessing

We employed both resting-state and 7-task fMRI data from the HCP S1200 release [74]. For each participant, resting-state fMRI scans were conducted over the course of two days. Each day included two separate 15-minute sessions (with eyes open and fixation), resulting in a total of four resting-state scans per individual. Within each day, the two resting-state scans utilized opposite phase-encoding directions: left-to-right (L/R) and right-to-left (R/L). Following the resting-state scans each day, participants completed 30 minutes of task fMRI data collection. The seven tasks—emotional, gambling, language, motor, relational reasoning, social, and working memory (N-back)—distributed across the two sessions, with each task administered twice using opposing phase-encoding directions (L/R and R/L). Detailed descriptions of the resting-state and task fMRI data collection protocols are available in prior publications [54, 75].

All imaging data were collected at Washington University in St. Louis using a customized Siemens 3T Skyra scanner, which utilized a multiband sequence for rapid image acquisition. Structural images were obtained at 0.7-mm isotropic resolution. Resting-state fMRI data were collected with 2-mm isotropic spatial resolution and a repetition time (TR) of 0.72 seconds. Further details regarding data acquisition and preprocessing pipelines are described elsewhere [74, 75]. Informed consent was obtained from all participants, and all procedures adhered to relevant ethical guidelines and regulations.

For the resting-state data, we utilized surface-based CIFTI fMRI scans that were registered using MSMAll and had been preprocessed with the HCP's ICA-based artifact removal process (ICA-FIX) to minimize the effects of spatially structured noise [75]. For the task-based data, we utilized MSMAll-registered fMRI scans that were minimally preprocessed.

Both resting-state and task-state fMRI scans were spatially parcellated using a comprehensive brain-wide parcellation scheme. This scheme combined the Glasser cortical parcellation [41] with the Cole-Anticevic Brain-wide network partition for subcortical and cerebellar regions [42]. This approach resulted in a set of ROIs covering both cortical and subcortical areas, specifically yielding 360 cortical parcels and 358 subcortical and cerebellar parcels. However, we identified two ROIs from the Cole-Anticevic Brain-wide Network Partition that exhibited negligible variance (variance < 0.001), indicating a lack of data in these regions. These ROIs were key value 1040 labeled "Visual1-14_R-Caudate" and key value 7290 labeled "Frontoparietal-29_R-Cerebellum." Consequently, we excluded these two ROIs from further analysis. In summary, our final parcellation scheme consisted of 360 cortical ROIs and 356 subcortical and cerebellar ROIs, totaling 716 regions that were used for subsequent analyses.

Temporal preprocessing involved applying a zero-phase Butterworth band-pass filter with a frequency range of 0.01–0.1 Hz to the data to eliminate low frequency signal drifts and physiological noise [76, 77]. For the task-state fMRI scans, we additionally regressed out 24 motion parameters and task-related activations before band-pass filtering to control for head motion artifacts and the mere effects of brain-wide task-related coactivation. The task-related activations were modeled by convolving boxcar regressors—constructed from task onset and duration information—with a hemodynamic response function. This regression was performed using the ordinary least squares method. No temporal normalization (e.g., z-scoring or variance normalization) was applied to either the resting-state or task-state datasets to preserve the original amplitude of the BOLD signals.

Group-level DMD

We first estimated the group-level causal connectivity matrix $A \in \mathbb{R}^{N \times N}$, which best describes

the causal relationships between temporally adjacent BOLD activations across all subjects:

$$\boldsymbol{x}_s(t) = A\boldsymbol{x}_s(t-1)$$

where $\boldsymbol{x}_s(t) \in \mathbb{R}^N$ represents the BOLD activation vector at time t for the *s*-th subject, and *N* denotes the number of ROIs.

Our objective was to find the matrix *A* that minimizes the cumulative prediction error across all subjects and time points:

$$F = \sum_{s=1}^{S}\sum_{t=2}^{T}\|\boldsymbol{x}_s(t) - A\boldsymbol{x}_s(t-1)\|^2$$

where *S* is the total number of subjects, *T* is the number of time points per subject, and $\|\cdot\|$ denotes the Euclidean norm.

To solve this optimization problem efficiently, we constructed two data matrices by concatenating the BOLD activation vectors across all subjects and time points: $X \in \mathbb{R}^{N\times S(T-1)}$ constructed by stacking $\boldsymbol{x}_s(t-1)$ for all subject $s \in \{1,2,\cdots,S\}$ and time points $t \in \{2,3,\cdots,T\}$ and $X' \in \mathbb{R}^{N\times S(T-1)}$ constructed by stacking $\boldsymbol{x}_s(t)$. Specifically, the two matrices are like the followings:

$$X = [\boldsymbol{x}_1(1), \boldsymbol{x}_1(2), \cdots, \boldsymbol{x}_1(T-1), \boldsymbol{x}_2(1), \cdots, \boldsymbol{x}_S(T-1)]$$

$$X' = [\boldsymbol{x}_1(2), \boldsymbol{x}_1(3), \cdots, \boldsymbol{x}_1(T), \boldsymbol{x}_2(2), \cdots, \boldsymbol{x}_S(T)]$$

The optimal matrix *A* that minimizes *F* can then be obtained using the least-squares solution [78, 79]:

$$A = X'X^+$$

where X^+ is the Moore-Penrose pseudoinverse of X.

However, measurement noise can introduce significant systematic bias in the DMD results because the above approach only minimizes the errors in X', implicitly assuming that there is no measurement error in *X*. To mitigate this bias, we employed the forward-backward DMD algorithm, which provides a simple yet effective method to reduce noise-induced bias [43]. The

forward-backward DMD approach operates on the premise that the effect of measurement noise on DMD is stable and systematic. In addition to estimating the forward dynamics $\boldsymbol{x}_s(t) = A\boldsymbol{x}_s(t-1)$, we also approximate the inverse dynamics:

$$\boldsymbol{x}_s(t-1) = B\boldsymbol{x}_s(t)$$

where $B \in \mathbb{R}^{N\times N}$ is another matrix to be estimated.

By computing both A and B, we can calculate a new, less-biased estimate of the system dynamics:

$$A_{\text{new}} = (AB^{-1})^{1/2}$$

where $(\cdot)^{1/2}$ denotes the matrix square root. This method leverages the systematic but opposite biases in A and B to achieve a more accurate estimation of the true system's DMs. To compute B, we utilized the data matrices in reverse order and solved:

$$B = XX'^{+}.$$

Finally, we calculated the improved estimate A_{new} using the formula above and performed an eigenvalue decomposition to obtain the group-level DMs ($\boldsymbol{\phi}_k$, complex eigenvectors) and their evolution coefficients (λ_k, corresponding complex eigenvalues):

$$A_{\text{new}}\boldsymbol{\phi}_k = \lambda_k\boldsymbol{\phi}_k$$

where k is eigenvalue index. Since A_{new} is a real value matrix, its complex eigenvalues and eigenvectors occur in conjugate pairs. This property ensures that when reconstructing the BOLD signals, the imaginary parts cancel out, resulting in real-valued activations. Each pair of conjugate eigenvectors corresponds to one dynamic mode, capturing oscillatory patterns in the data [45]. Prior to applying DMD, we down-sampled the fMRI data from the original TR of 0.72 seconds to a TR of 1.5 seconds using cubic spline interpolation (implemented in MATLAB) to reduce data complexity while enhancing the detection of meaningful dynamic differences due to the inherently slow hemodynamic responses.

The complex eigenvalues λ_k, referred to as "group-level (temporal) evolution coefficients" of the k-th DM, can be expressed in polar form using two real numbers: magnitude r and phase θ, such that $\lambda_k = re^{i\theta}$. Due to the properties of eigenvectors, if the initial BOLD activation is $\boldsymbol{x}_s(0) = \boldsymbol{\phi}_k$, then after 1TR, $\boldsymbol{x}_s(1) = A\boldsymbol{\phi}_k = \lambda_k\boldsymbol{\phi}_k = re^{i\theta}\boldsymbol{\phi}_k$; after 2TR, $\boldsymbol{x}_s(2) = A\boldsymbol{x}_s(1) = A(\lambda_k\boldsymbol{\phi}_k) = {\lambda_k}^2\boldsymbol{\phi}_k = r^2e^{2i\theta}\boldsymbol{\phi}_k$; and so on.

In this context, the magnitude of the evolution coefficient r indicates the proportion of the signal that persists after one TR, reflecting the stability or sustained influence of the DM. We will refer to this as "*persistence rate*." A higher persistence rate indicates that the DM maintains its influence over time, suggesting more stable or enduring neural activity within that mode. Meanwhile, the phase θ determines the rate at which the DM evolves. Specifically, the period of oscillation is given by $2\pi/\theta$ TRs, which quantifies the speed of signal propagation. We will refer to this as "*temporal progression rate*" or "*progression rate*." A higher temporal progression rate signifies faster oscillatory dynamics, indicating quicker changes in the neural activity patterns associated with that mode.

Subject-level estimation of DM metrics

Building upon the understanding that the fundamental organizational principles and large-scale network architectures of the human brain are remarkably consistent across individuals [80, 81], we modeled the subject-level fMRI dynamics using the same set of large-scale signal propagation modes—i.e., DMs derived from group-level analysis—across all individuals, while allowing for variations in the propagation strength and speed unique to each subject.

To this end, we decomposed each subject's causal BOLD signal dynamics into the temporal evolution of the DMs. Specifically, for each subject s and given K DMs, the BOLD signal at time $t-1$, $\boldsymbol{x}_s(t-1)$, can be decomposed as:

$$\boldsymbol{x}_s(t-1) = \sum_{k=1}^{K} [b_k(t-1)\boldsymbol{\phi}_k + b_k(t-1)^* \boldsymbol{\phi}_k^*] + \boldsymbol{\varepsilon}(t-1)$$

where the coefficient $b_k(t-1)$, referred to as "projection coefficient", of group-level DM vector $\boldsymbol{\phi}_k$ is estimated by projecting the BOLD activation vector $\boldsymbol{x}_s(t-1)$ onto the DM vector space, reflecting engagement level of the k-th DM's activation at time $t-1$. $b_k(t-1)^*$ and $\boldsymbol{\phi}_k^*$ are complex conjugate of $b_k(t-1)$ and $\boldsymbol{\phi}_k$. The residual $\boldsymbol{\varepsilon}(t-1)$ is the orthogonal component remaining after this projection of $\boldsymbol{x}_s(t-1)$.

Assuming that the global structure of signal propagation for each DM is preserved, the subsequent BOLD signal can be modeled as:

$$\hat{\boldsymbol{x}}_s(t|t-1) = \sum_{k=1}^{2K} [d_k b_k(t-1)\boldsymbol{\phi}_k + d_k^* b_k(t-1)^* \boldsymbol{\phi}_k^*] + d_0 \varepsilon(t-1)$$

where d_k are subject-specific evolution coefficients representing the persistence and progression rates for each mode in that subject's brain (see previous section), and d_0 is an additional subject-specific (autocorrelation) coefficient accounting for autocorrelation in the residual. $\hat{\boldsymbol{x}}_s(t|t-1)$ is the predicted BOLD signal at time t based on information up to time $t-1$. Essentially, we modeled the subject-level fMRI dynamics using the same large-scale signal propagation modes across individuals, allowing for variations in propagation strength and speed. Our objective is therefore to determine the evolution coefficients d_k and d_k^* $(k = 0,1,2,\cdots,K)$ that best approximate the predicted signal $\hat{\boldsymbol{x}}_s(t|t-1)$ to the actual observed signal $\boldsymbol{x}_s(t)$.

To solve this problem, we reorganized it using matrix notation. Let $\Phi \in \mathbb{C}^{N\times M}$ denote the complex matrix whose columns are the eigenvectors corresponding to the selected DMs, where N is the number of ROIs and $M = 2K$ accounts for complex conjugate pairs of eigenvectors (since the eigenvalues and eigenvectors of real matrices appear in complex conjugate pairs).

For each subject s, we approximated their fMRI causal dynamics as a combination of the

selected DMs modulated by subject-specific evolution coefficients. Specifically, we modeled the dynamics as:

$$\boldsymbol{x}_s(t) \approx (d_0(I - \Phi\Phi^+) + \Phi D_s \Phi^+)\boldsymbol{x}_s(t-1)$$

where $\boldsymbol{x}_s(t) \in \mathbb{R}^N$ represents the BOLD activation vector at time t for the *s*-th subject, *I* is the identity matrix of size *N*-by-*N*, $D_s = \begin{bmatrix} d_1 & 0 & 0 & 0 & 0 \\ 0 & d_1^* & 0 & 0 & 0 \\ 0 & 0 & \ddots & 0 & 0 \\ 0 & 0 & 0 & d_K & 0 \\ 0 & 0 & 0 & 0 & d_K^* \end{bmatrix}$ is a diagonal matrix containing the subject-specific evolution coefficients d_k, and d_0 represents the autocorrelation coefficient of the orthogonal complement of the column space of Φ. In this formulation, $\Phi\Phi^+$ is the projection matrix onto the subspace spanned by the selected DMs, and $(I - \Phi\Phi^+)$ projects onto the orthogonal complement of that subspace. Thus, the term $d_0(I - \Phi\Phi^+)\boldsymbol{x}_s(t-1)$ accounts for the residual dynamics not captured by the selected DMs.

Our objective was to estimate the evolution coefficients d_k for $k = 0,1,\cdots,K$ that minimize the cumulative prediction error across all time points for each subject:

$$F_s = \sum_{t=2}^{T} \|\boldsymbol{x}_s(t) - (d_0(I - \Phi\Phi^+) + \Phi D_s \Phi^+)\boldsymbol{x}_s(t-1)\|^2$$

where T is the total number of time points.

To minimize F_s, we formulated the problem as solving a system of linear equations. This was achieved by expanding F_s and setting the partial derivatives (see Supplementary Result 2) with respect to each d_k to zero, resulting in the following linear system:

$$Z \begin{bmatrix} d_0 \\ d_1 \\ d_1^* \\ \vdots \\ d_K \\ d_K^* \end{bmatrix} = \boldsymbol{w}$$

where $Z \in \mathbb{C}^{(2K+1)\times(2K+1)}$ is a square matrix, and $\boldsymbol{w} \in \mathbb{C}^{(2K+1)}$ is the right-hand side vector.

The elements of Z and $\boldsymbol{w}$ are defined based on the data $\boldsymbol{x}_s(t)$ and the projections onto the subspace spanned by Φ and its orthogonal complement.

For Z $(i, j \in [1,2,\cdots,2K])$:

$$z_{00} = \sum_{t=2}^{T} \boldsymbol{x}_s(t-1)^{\dagger}(I - \Phi\Phi^{+})^{\dagger}(I - \Phi\Phi^{+})\boldsymbol{x}_s(t-1)$$

$$z_{0i} = \sum_{t=2}^{T} \boldsymbol{x}_s(t-1)^{\dagger}(I - \Phi\Phi^{+})^{\dagger}\, \boldsymbol{u}_i \boldsymbol{v}_i^{\dagger} \boldsymbol{x}_s(t-1)$$

$$z_{0i} = z_{i0}^{\dagger}$$

$$z_{ij} = \sum_{t=2}^{T} \boldsymbol{x}_s(t-1)^{\dagger}\left(\boldsymbol{v}_i \boldsymbol{u}_i^{\dagger} \boldsymbol{u}_j \boldsymbol{v}_j^{\dagger}\right)\boldsymbol{x}_s(t-1)$$

For $\boldsymbol{w}$ $(i \in [1,2,\cdots,2K])$:

$$w_0 = \sum_{t=2}^{T} \boldsymbol{x}_s(t-1)^{\dagger}(I - \Phi\Phi^{+})^{\dagger}\boldsymbol{x}_s(t)$$

$$w_i = \sum_{t=2}^{T} \boldsymbol{x}_s(t-1)^{\dagger}\boldsymbol{v}_i \boldsymbol{u}_i^{\dagger}\boldsymbol{x}_s(t)$$

where $\boldsymbol{u}_i$ is i-th column vector of Φ, and $\boldsymbol{v}_i$ is i-th column vector of $(\Phi^{+})^{\dagger}$, where $\dagger$ denotes conjugate transpose. By solving this linear system for each subject, we obtained the subject-specific coefficients:

$$\begin{bmatrix} d_0 \\ d_1 \\ d_1^{*} \\ \vdots \\ d_K \\ d_K^{*} \end{bmatrix} = Z^{-1}\boldsymbol{w}.$$

The detailed derivation of the linear system and the definitions of Z and $\boldsymbol{w}$ are provided in Supplementary Result 2.

Subsequently, we can derive the subject-specific persistence rate (r_k) and progression rate

(θ_k) can be achieved from the evolution parameters, expressed as $d_k = r_k e^{i\theta_k}$ for $k = 1,2,\cdots,K$. It is important to note that while the persistence rates from d_k and its complex conjugate $d_k^* = r_k e^{-i\theta_k}$ are same as r_k, the progression rates have opposite signs (θ_k and $-\theta_k$, respectively). Therefore, we exclusively use d_k (i.e., not d_k^*) for estimating the DM metrics.

Additionally, we estimated the subject-specific *mode-engagement level*, $\bar{b}_k = \frac{1}{T-1}\sum_{t=2}^{T}|b_k(t-1)|$, which indicates how dominantly the *k*-th DM is engaged during the fMRI scan. The projection coefficient, $b_k(t-1)$, can be obtained by applying Φ^+ to $\boldsymbol{x}_s(t-1)$:

$$\begin{bmatrix} b_1(t-1) \\ b_1(t-1)^* \\ b_2(t-1) \\ b_2(t-1)^* \\ \vdots \end{bmatrix} = \Phi^+ \boldsymbol{x}_s(t-1).$$

For the resting-state data, we utilized the down-sampled fMRI scans with a TR of 1.5 seconds, as described in the previous section. In contrast, we did not down-sample the task-state data due to the limited number of time points available in these datasets. Therefore, when comparing the DM coefficients between the resting-state and task-state data, we adjusted the resting-state DM coefficients to ensure temporal consistency between the two datasets. Specifically, we scaled the resting-state DM coefficients by raising them to the power of 0.72/1.5, accounting for the difference in TRs (1.5 seconds for resting-state and 0.72 seconds for task-state data). By making this adjustment, we ensured that the resting-state DM coefficients, originally reflecting temporal evolution over 1.5 seconds, were scaled appropriately to match the temporal evolution over 0.72 seconds represented in the task-state DM coefficients.

Optimizing the number of DMs

To determine the optimal number of DMs for accurately describing brain-wide BOLD dynamics, we employed a 5-fold cross-validation approach that evaluated predictive performance across models with increasing numbers of DMs. The number of DMs was incremented by sequentially including those with group-level DM evolution coefficients with large magnitudes (λ_k; see "Group-level DMD" section), reflecting their relative contribution to the group-level dynamics. In each fold, the training set was used to estimate the group-level DMs ($\boldsymbol{\phi}_k$). For the test set, each subject's resting-state fMRI run was divided into two segments: (1) test-fitting data (first four-fifths, 12 minutes) — which used to estimate the subject-specific DM coefficients (d_k); (2) test-validation data (remaining one-fifth, 3 minutes) — which was reserved for assessing predictive ability.

Predictive performance was evaluated by measuring the prediction error based on the entire history within the test-validation segment for each subject in the test set. The prediction error was defined as:

$$\boldsymbol{\varepsilon}(t) = \boldsymbol{x}(t) - \hat{\boldsymbol{x}}(t|t-1)$$

where $\boldsymbol{x}(t)$ is the observed BOLD activation vector at time t, and $\hat{\boldsymbol{x}}(t|t-1)$ is the one-step-ahead prediction based on the DM coefficients fitted using the test-fitting data (see previous section).

For normalization, we utilized the R^2 measure, which quantifies the proportion of variance in the signal that the model can explain. To account for varying variance across ROIs, we calculated R^2 for each ROIs and averaged them:

$$R^2 = \sum_{n=1}^{N} R_n^2 = \frac{1}{N}\sum_{n=1}^{N}\left(1 - \frac{\sum_{t=2}^{T} \varepsilon_n(t)^2}{\sum_{t=2}^{T}[x_n(t) - \bar{x}_n]^2}\right)$$

where $x_n(t)$ is the BOLD activation of the *n*-th ROI at time t, $\varepsilon_n(t)$ is the prediction error for the *n*-th ROI at time t, and $\bar{x}_n$ is the mean BOLD activation over time for the *n*-th ROI,

calculated as: $\bar{x}_n = \frac{1}{T-1}\sum_{t=2}^{T} x_n(t)$.

This R^2 measure was calculated for every subject in the test set of each fold, then averaged across the five folds, and subsequently used to compare model performance.

Null model

To establish a baseline for model comparison, we used a null AR(1) model that accounts solely for the autocorrelation between temporally adjacent signals:

$$\boldsymbol{x}(t) = d_0\boldsymbol{x}(t-1) + \boldsymbol{\varepsilon}(t)$$

where d_0 is the scalar autocorrelation coefficient and $\boldsymbol{\varepsilon}(t)$ represents white noise error terms. The optimal estimation of d_0 is achieved using the following equation:

$$d_0 = \frac{\sum_{t=2}^{T} \boldsymbol{x}(t-1)^{\dagger}\boldsymbol{x}(t)}{\sum_{t=2}^{T} \boldsymbol{x}(t-1)^{\dagger}\boldsymbol{x}(t-1)}$$

where $\boldsymbol{x}(t-1)^{\dagger}$ represents the (complex conjugate) transpose of $\boldsymbol{x}(t-1)$.

Note that this null AR(1) model achieved a higher cross-validated R^2 of 0.7767 compared to the zero-order random walk model ($\boldsymbol{x}(t) = \boldsymbol{x}(t-1) + \boldsymbol{\varepsilon}(t)$), which achieved an R^2 of 0.7618.

Sparse linear model

In previous comparisons utilizing state-of-the-art models to characterize macroscopic BOLD dynamics [44], simple linear models consistently demonstrated the best fit for resting-state BOLD timeseries. These linear models capture the differences in BOLD signals between adjacent time points (t and $t-1$) by employing a linear combination of signals from the preceding time point ($t-1$). Building on the superior performance of the null AR(1) model, our approach models the residual variance not accounted for by the null AR(1) model through a linear combination of signals at the previous time point:

$$\boldsymbol{x}(t) - d_0\boldsymbol{x}(t-1) = W\boldsymbol{x}(t-1) + \boldsymbol{\varepsilon}(t)$$

where W is an *N*-by-*N* matrix representing effective connectivity between ROIs, d_0 is the scalar autocorrelation coefficient which is estimated identically to the null model, and $\boldsymbol{\varepsilon}(t)$ represents white noise error terms.

Due to the increased number of ROIs in our current study, estimating a dense linear model became infeasible. Thus, we employed a sparse modeling approach using LASSO regularization with a hyperparameter Γ. We estimated Γ by evaluating training data across a range of values $[10,20,30,\cdots,100]$ within each cross-validation fold. The optimal Γ was determined by interpolating the achieved cross-validated R^2 values (estimated within the training dataset) across this range (with cubic spline interpolation) and subsequently applied to the test data (see Supplementary Figure 2a).

Nonlinear manifold-based model

In the previous study [44], the manifold-based model achieved comparable fit for BOLD timeseries data among non-linear models. The manifold-based model uses the characteristics of manifold that can be approximated by a linear hyperplane in the small vicinity of a given point. We used the local polynomial modelling of order 1 [82] that is used in the previous work [44] but also with modification to model the residual variance not accounted for by the null AR(1) model:

$$\boldsymbol{x}(t) - d_0\boldsymbol{x}(t-1) = f(\boldsymbol{z}) \approx \boldsymbol{c}_v + W_v[\boldsymbol{z} - \boldsymbol{x}(t_v - 1)]$$

where the function $f(\boldsymbol{z})$ is approximated as a linear function in the vicinity of $\boldsymbol{x}(t_l - 1)$. The constant vector $\boldsymbol{c}_v$ and matrix W_v were estimated from the test-fitting data $\boldsymbol{x}(t_f - 1)$, but weighted according to its distance to $\boldsymbol{x}(t_v - 1)$ with a gaussian kernel:

$$k\left(\boldsymbol{x}(t_f - 1), \boldsymbol{x}(t_v - 1)\right) = \frac{1}{\sqrt{2\pi h}} \exp\left(-\frac{\left\|\boldsymbol{x}(t_f - 1) - \boldsymbol{x}(t_v - 1)\right\|^2}{2h^2}\right)$$

The hyperparameter h controls the degree of locality in the model. We estimated h by evaluating training data across a range of values $[2,4,6,\cdots,20]$ within each cross-validation fold. The optimal h was determined by interpolating the achieved cross-validated R^2 values (estimated within the training dataset) across this range (with cubic spline interpolation) and subsequently applied to the test data (see Supplementary Figure 2b).

For detailed methodology on the weighted least squares estimation used to solve this model, please refer to Nozari, Bertolero [44].

Group-level FC topography

FC was determined by calculating Pearson correlations from each subject's preprocessed ROI time-series without applying GSR. Specifically, FC was computed between 360 cortical regions for each subject, followed by Fisher's r-to-z transformation (arctanh). These transformed FC values were then averaged across all subjects and converted back to correlation coefficients within the range of [−1, 1] using the tanh function.

TVFC measure (std)

To assess the temporal variability of FC, we computed the std of TVFC using a sliding window method with a window size of w = 63 TRs (45.36 seconds). Prior to applying the sliding window approach, we performed high-pass filtering to remove frequency components below $1/w$ (where w is the window size in seconds) in addition to the previously applied bandpass filtering (0.01–0.1 Hz) to eliminate spurious fluctuations in TVFC [83]. Within each sliding window, Pearson correlation coefficients were computed for all pairs of cortical ROIs. The std of these TVFC time series for each ROI was then determined to quantify the temporal variability of FC.

Reconstructed FC and TVFC matrices using DMs

To reconstruct the FC matrix, we aggregated contributions from the top five DMs. For each DM, we generated time series for all 360 cortical regions by normalizing the group-level DM evolution coefficients (λ_k) to unit magnitude, thereby preserving only phase information, and applied these coefficients across 10,000 time points with a temporal resolution of 0.5 seconds. The time series for the *n*-the ROI in the *k*-th DM were reconstructed using the formula:

$$x_n(t) = e^{\theta_k \cdot t/\Delta T}(\phi_k)_n + e^{-\theta_k \cdot t/\Delta T}(\phi_k^*)_n$$

where $(\phi_k)_n$ is the *n*-th element of the *k*-th DM vector ϕ_k, θ_k is the phase (argument) of the group-level DM coefficient λ_k, and ΔT is the resampled TR used in the group-level DMD ($\Delta T = 1.5s$).

The five reconstructed time (i.e., one per each DM) series were then weighted and averaged based on the group-averaged mode engagement level of each DM ($\overline{|b_k|}$). The FC matrix was subsequently computed by calculating Pearson correlation coefficients between all pairs of the averaged ROI time series. The TVFC (i.e., std) matrix was computed by calculating the std of FCs estimated using a sliding window approach, employing the same window size as used in the original TVFC analysis. To assess the similarity of the reconstruction, we correlated the lower triangular elements of the reconstructed FC matrix (or reconstructed TVFC matrix) with those of the original FC matrix (or original TVFC matrix).

Network community analysis

For identify community structure, we applied the Newman's spectral community detection implemented in Brain Connectivity Toolbox [84] with a resolution parameter set to 1 to both the original FC matrix and a reconstructed FC matrix derived from the DMs.

FC gradients (cortical areas)

Following the methodology of the previous study [5], the group-level cortical FC matrix was thresholded to retain only the top 20% of values before extracting the gradients to consider most significant connections. Then, resting-state FC gradients were obtained by performing PCA on the group-level cortical FC matrix.

Subcortical and cerebellar FC-based functional gradients

Due to the lower signal-to-noise ratio of BOLD signals in non-neocortical regions compared to neocortical areas, we employed connectopic mapping [37] to characterize the functional organization of subcortical structures using resting-state fMRI data. This approach involves calculating the FC profiles between subcortical ROIs and other brain areas, followed by assessing the similarities of these FC profiles among subcortical ROIs. Subsequently, a dimensionality reduction technique is applied to the similarity matrix to derive spatial topographies that account for the most variance.

We applied this methodology to obtain the functional gradients of the hippocampus, amygdala, thalamus, striatum, brain stem, and cerebellum. For each subcortical area, let there be N ROIs within the area and M ROIs outside of it. For each subject, we computed the group-level FC matrix between the subcortical ROIs and external ROIs and then averaged these matrices across subjects to obtain a group-level FC topography. This process resulted in an M-by-N FC matrix, where each column represents the FC profile of a subcortical ROI. We then calculated the pairwise Pearson correlations between all subcortical ROIs, generating an N-by-N similarity (i.e., correlation) matrix. PCA was performed on this similarity matrix, and the first principal component, representing the principal functional gradient of the subcortical area, was retained. The same methodology was applied to the cerebellum to derive its functional gradient.

The resulting spatial topographies of the functional gradients for the subcortical areas and the cerebellum are illustrated in Supplementary Figure 7.

Lag projection

We employed the lag analysis algorithm as outlined by Raut, Mitra [85] on all cortical ROI time-series. Specifically, the time-lag between each pair of cortical ROI time series was determined by identifying the peak of their lagged cross-covariance function [39]. The lag projections were then calculated by averaging the pair-wise time-lag values across each column of the resulting time-lag matrix for all cortical ROIs.

Quasi-periodic pattern (QPP)

QPPs were identified using the template matching algorithm described by Majeed, Magnuson [46]. The cortical ROI time-series from each subject were concatenated, and a random window of BOLD timepoints was selected as the initial QPP template. The algorithm then calculated the sliding correlation between the concatenated ROI time-series and this template. During the first two iterations, a correlation threshold of 0.1 was applied, which was increased to 0.2 for subsequent iterations. Peaks in the thresholded correlation time series were detected, and the corresponding time-series segments were averaged to update the QPP template. This iterative process was repeated until the template remained unchanged for two consecutive iterations ($r > 0.9999$). The algorithm was executed ten times, and the template with the highest average sliding window correlation across all iterations was selected as the final QPP template. QPP identification was performed on time series with and without GSR. GSR was performed by regressing the global mean time series—calculated as the average across all cortical vertices—onto each individual cortical time series.

Correlation between the global signal and the projected signal onto DMs

The global signal time series was derived by averaging the time series of all ROIs. To obtain the projected signal onto k-th DM, we first calculated the coefficient $b_k(t-1)$ for each time point and multiplied it by the group-level DM vector $\boldsymbol{\phi}_k$ (i.e., $b_k(t-1)\boldsymbol{\phi}_k$). The real components of the resulting products were then averaged to generate the global activity of the projected signal for the k-th DM. Finally, we computed the correlation between the global signal time series and the global activity time series of the projected signal for each subject.

Seed-based FC

FC was calculated using ROI time series with the application of GSR. GSR was performed by regressing the global mean time series—calculated as the average across all cortical vertices—onto each individual cortical time series. The residuals from these regressions were then utilized for determining FCs. FCs were determined by calculating Pearson correlations between the residual time series of each seed ROI and those of the other cortical ROIs.

Yeo's 7-network partition

The 7-network parcellation of the cortical areas was performed following Yeo, Krienen [81]. For this analysis, we used the group FC matrix (within cortical areas) with GSR. Each ROI's connectivity profile was z-score normalized across all ROIs to ensure standardized data. K-means clustering was then applied to the normalized connectivity profiles, specifying seven clusters with 10 replicates to enhance clustering stability. The resulting clusters corresponded to two DMNs (possibly reflecting sub-networks of DMN), the CEN, SM, visual, dorsal attention, and ventral attention networks. The cluster centroids were utilized to represent the spatial distribution of each respective network. Supplementary Figure 5 illustrates the spatial topographies of each cluster centroid.

Laterality index (LI)

To evaluate the hemispheric lateralization throughout the scanning period, we calculated the LI for each ROI. Specifically, we used the mean laterality index (MLI), which is the average of the dynamic laterality index (DLI) values across all sliding time windows as defined by Wu, Kong [40]. The procedure is outlined below.

Initially, we calculated the DLI for each ROI within sliding time windows of $w = 30$ seconds (~41.6TRs) with a 10-second sliding interval (Δw). The DLI was defined using a global signal-based approach. Specifically, for the n-th ROI during the time window starting at time t, the DLI was computed as the difference between its Pearson correlation with the left hemispheric global signal ($\mathrm{GS_L}$) and its correlation with the right hemispheric global signal ($\mathrm{GS_R}$):

$$\mathrm{DLI}_n(t) = R\big(x_n(t{:}\,t+w), \mathrm{GS_L}(t{:}\,t+w)\big) - R\big(x_n(t{:}\,t+w), \mathrm{GS_R}(t{:}\,t+w)\big)$$

where $x_n(t{:}\,t+w)$ represents the BOLD time series of the n-th ROI within the time window from t to $t+w$. $\mathrm{GS_L}(t{:}\,t+w)$ and $\mathrm{GS_R}(t{:}\,t+w)$ denote the global signals of the left and right hemispheres, respectively, within the same time window. These are calculated as the averaged BOLD time series of all ROIs within each hemisphere. $R(\cdot,\cdot)$ denotes the Pearson correlation coefficient.

A positive DLI indicates that the ROI's activity is more synchronized with the left hemisphere (leftward laterality), while a negative DLI indicates stronger synchronization with the right hemisphere (rightward laterality).

The MLI for each ROI was derived by averaging its DLI values across all sliding time windows:

$$\mathrm{MLI}_n = \frac{1}{\lfloor T/\Delta w \rfloor} \sum_{t=0,\Delta w,2\Delta w,\cdots} \mathrm{DLI}_n(t)$$

where T is the total number of time points, $\lfloor\cdot\rfloor$ is the floor function, $\lfloor T/\Delta w \rfloor$ is the total

number of sliding time windows, $\mathrm{DLI}_n(t)$ is the DLI of n-th ROI at time window t. Thus, MLI indicates each ROI's average hemispheric lateralization over the entire scan duration.

Behavior analysis

For our factor analysis, we utilized the Python script provided by Schöttner, Bolton [53]. This script conducts hierarchical factor analysis on the dataset to identify underlying latent variables, employing maximum likelihood estimation in conjunction with orthogonal (varimax) rotation. Running this script generates factor analysis results across various numbers of latent dimensions. We opted for a four-factor model due to its previously demonstrated robustness [53].

The four factors derived from the HCP dataset represent distinct dimensions of behavior. (1) Mental health reflects a spectrum of emotional well-being, encompassing positive states like life satisfaction and social support alongside challenges such as anxiety and depression. (2) Cognition captures intellectual abilities across various domains, including memory, reasoning, and language, indicating overall cognitive function. (3) Processing speed measures the efficiency of cognitive processing, emphasizing quick responses and reaction times, which contribute to cognitive performance in diverse tasks. (4) Substance use represents tendencies toward alcohol, tobacco, and drug use, highlighting behavioral patterns that can influence physical and mental health.

To examine the relationships between these behavioral factors and DM metrics while controlling for potential confounds, we performed general linear model (GLM) analyses using an ANCOVA approach. The confounding variables included in the model were age, sex, handedness, and the cube roots of ICV and TGMV.

Given the multiple comparisons involved in assessing all possible combinations of behavioral factors (four latent factors), DM metrics (five metrics), and metric types (three types:

engagement, persistence, and progression), we applied a FWE correction to our statistical assessments. To achieve this, we employed Smith's permutation testing method [86]. Specifically, all DM metrics were projected onto the vector space defined by the confounding variables and a constant term, retaining only the residuals. GLM analyses were then conducted using these residuals. To calculate FWE-corrected p-values, the residuals were permuted across subjects. In each permutation, GLM analyses were performed for all possible pairs of behavioral factors, DM metrics, and metric types, and the maximum absolute t-value was retained. This process was repeated for 10,000 permutations to generate a distribution of maximum absolute t-values, which was used to determine the p-values.

Heritability analysis

We utilized twin data from the HCP to assess the heritability of DMs. Participants lacking zygosity information or essential confound data (e.g., age, sex, structural information) were excluded, resulting in a sample of 998 individuals, including 104 monozygotic (MZ) twin pairs, 97 dizygotic (DZ) twin pairs, and 110 singletons. Zygosity information was employed to fit an ACE model, which decomposes the total phenotypic variance into three components: genetic factors (A, representing heritability), shared environmental (C), and unique environmental factors (E). The APACE permutation inference system [52] was applied using each subject's estimation of DM coefficient's magnitude and phases. For both magnitude and phase measures, we regressed out the effects of the following confounding: age, age squared, sex, the interaction between age and sex, the interaction between sex and age squared, body mass index (BMI), race, handedness, years of education, cube root of ICV and TGMV, mean frame-wise displacement. The ACE model was applied separately to the magnitude and phase of DM coefficients. Statistical significance (p-values) was determined using 5,000 permutations, and confidence intervals (CIs) were estimated through 1,000 bootstrap resamples.

We conducted cosine similarity analysis using the magnitude and phase measures after regressing out confounding variables.

Assessment of the significance of DM

If a specific DM is not significantly present in the subject's BOLD signal dynamics, the estimation of the argument (phase) of its corresponding DM coefficient d_k (i.e., progression rate) tends to be randomly distributed around zero. This randomness arises because, without a substantial presence of the DM in the subject's neural activity, there is insufficient information to consistently determine the direction of signal propagation associated with that DM. In such cases, the phase estimates do not carry meaningful information about the temporal evolution of the neural activity patterns within the mode.

Considering this, to assess whether each DM is significantly present (for the task-state data in the current study), we performed a one-sample t-test for each DM to determine if the mean phase significantly differs from zero across the subjects. A significant deviation from zero would indicate that the phase estimates are consistently oriented in a particular direction, suggesting a significant presence of the DM in the subject's brain activity.

Author contributions

Youngjo Song: Conceptualization, Data Curation, Methodology, Validation, Visualization, Formal Analysis, Writing – Original Draft.

Pyeong Soo Kim: Formal Analysis, Writing – Review & Editing.

Benjamin Philip: Writing – Review & Editing.

Taewon Kim: Supervised the study, Resources, Formal Analysis, Writing – Review & Editing.

Data availability

The resting-state and task-state fMRI data analyzed in this study are publicly accessible through the HCP S1200 Release. You can obtain the data at https://www.humanconnectome.org/study/hcp-young-adult/document/1200-subjects-data-release. For researchers interested in accessing restricted data, such as information on zygosity and parental details, please contact the HCP Project Manager and follow the application procedures outlined by the HCP at (https://www.humanconnectome.org/study/hcp-young-adult/document/restricted-data-usage) to obtain the data.

Code availability

All analyses in this study were conducted using MATLAB R2021a. The scripts and code supporting the study's findings are available on GitHub and will be publicly accessible upon the paper's publication.

References

1. Bressler, S.L. and V. Menon, *Large-scale brain networks in cognition: emerging methods and principles.* Trends in cognitive sciences, 2010. **14**(6): p. 277-290.
2. Hoel, E.P., L. Albantakis, and G. Tononi, *Quantifying causal emergence shows that macro can beat micro.* Proceedings of the National Academy of Sciences, 2013. **110**(49): p. 19790-19795.
3. Breakspear, M., *Dynamic models of large-scale brain activity.* Nature neuroscience, 2017. **20**(3): p. 340-352.
4. Shine, J.M., et al., *Human cognition involves the dynamic integration of neural activity and neuromodulatory systems.* Nature neuroscience, 2019. **22**(2): p. 289-296.
5. Margulies, D.S., et al., *Situating the default-mode network along a principal gradient of macroscale cortical organization.* Proceedings of the National Academy of Sciences, 2016. **113**(44): p. 12574-12579.
6. Goulas, A., K. Zilles, and C.C. Hilgetag, *Cortical gradients and laminar projections in mammals.* Trends in neurosciences, 2018. **41**(11): p. 775-788.
7. Mesulam, M.-M., *From sensation to cognition.* Brain: a journal of neurology, 1998. **121**(6): p. 1013-1052.
8. Raut, R.V., et al., *Global waves synchronize the brain's functional systems with*

fluctuating arousal. Science advances, 2021. **7**(30): p. eabf2709.
9. Gu, Y., et al., *Brain activity fluctuations propagate as waves traversing the cortical hierarchy.* Cerebral cortex, 2021. **31**(9): p. 3986-4005.
10. Vézquez-Rodríguez, B., et al., *Signal propagation via cortical hierarchies.* Network neuroscience, 2020. **4**(4): p. 1072-1090.
11. Friston, K., *A theory of cortical responses.* Philosophical transactions of the Royal Society B: Biological sciences, 2005. **360**(1456): p. 815-836.
12. Lanzoni, L., et al., *The role of default mode network in semantic cue integration.* NeuroImage, 2020. **219**: p. 117019.
13. Friston, K., *Functional integration and inference in the brain.* Progress in neurobiology, 2002. **68**(2): p. 113-143.
14. Choi, I., J.-Y. Lee, and S.-H. Lee, *Bottom-up and top-down modulation of multisensory integration.* Current Opinion in Neurobiology, 2018. **52**: p. 115-122.
15. Uddin, L.Q., et al., *Functional connectivity of default mode network components: correlation, anticorrelation, and causality.* Human brain mapping, 2009. **30**(2): p. 625-637.
16. Van den Heuvel, M.P. and O. Sporns, *Network hubs in the human brain.* Trends in cognitive sciences, 2013. **17**(12): p. 683-696.
17. Gordon, E.M., et al., *Three distinct sets of connector hubs integrate human brain function.* Cell reports, 2018. **24**(7): p. 1687-1695. e4.
18. Menon, V. and M. D'Esposito, *The role of PFC networks in cognitive control and executive function.* Neuropsychopharmacology, 2022. **47**(1): p. 90-103.
19. Vincent, J.L., et al., *Evidence for a frontoparietal control system revealed by intrinsic functional connectivity.* Journal of neurophysiology, 2008. **100**(6): p. 3328-3342.
20. Menon, V., *20 years of the default mode network: A review and synthesis.* Neuron, 2023. **111**(16): p. 2469-2487.
21. Yousefi, B., et al., *Quasi-periodic patterns of intrinsic brain activity in individuals and their relationship to global signal.* Neuroimage, 2018. **167**: p. 297-308.
22. Abbas, A., et al., *Quasi-periodic patterns contribute to functional connectivity in the brain.* Neuroimage, 2019. **191**: p. 193-204.
23. Fox, M.D., et al., *The human brain is intrinsically organized into dynamic, anticorrelated functional networks.* Proceedings of the National Academy of Sciences, 2005. **102**(27): p. 9673-9678.
24. Seeley, W.W., *The salience network: a neural system for perceiving and responding to homeostatic demands.* Journal of Neuroscience, 2019. **39**(50): p. 9878-9882.
25. Menon, V. and L.Q. Uddin, *Saliency, switching, attention and control: a network model of insula function.* Brain structure and function, 2010. **214**: p. 655-667.
26. Sridharan, D., D.J. Levitin, and V. Menon, *A critical role for the right fronto-insular cortex in switching between central-executive and default-mode networks.* Proceedings of the National Academy of Sciences, 2008. **105**(34): p. 12569-12574.
27. Goulden, N., et al., *The salience network is responsible for switching between the default mode network and the central executive network: replication from DCM.* Neuroimage, 2014. **99**: p. 180-190.
28. Weissman, D.H., et al., *The neural bases of momentary lapses in attention.* Nature neuroscience, 2006. **9**(7): p. 971-978.
29. Kelly, A.C., et al., *Competition between functional brain networks mediates behavioral variability.* Neuroimage, 2008. **39**(1): p. 527-537.
30. Menon, V., *Large-scale brain networks and psychopathology: a unifying triple network model.* Trends in cognitive sciences, 2011. **15**(10): p. 483-506.

31. Kutz, J.N., et al., *Dynamic mode decomposition: data-driven modeling of complex systems*. 2016: SIAM.
32. Iungo, G.V., et al. *Data-driven reduced order model for prediction of wind turbine wakes*. in *Journal of Physics: Conference Series*. 2015. IOP Publishing.
33. Kuttichira, D.P., et al. *Stock price prediction using dynamic mode decomposition*. in *2017 International Conference on Advances in Computing, Communications and Informatics (ICACCI)*. 2017. IEEE.
34. Lu, H. and D.M. Tartakovsky, *Prediction accuracy of dynamic mode decomposition.* SIAM Journal on Scientific Computing, 2020. **42**(3): p. A1639-A1662.
35. Barocio, E., et al., *A dynamic mode decomposition framework for global power system oscillation analysis.* IEEE Transactions on Power Systems, 2014. **30**(6): p. 2902-2912.
36. Proctor, J.L., S.L. Brunton, and J.N. Kutz, *Dynamic mode decomposition with control.* SIAM Journal on Applied Dynamical Systems, 2016. **15**(1): p. 142-161.
37. Haak, K.V., A.F. Marquand, and C.F. Beckmann, *Connectopic mapping with resting-state fMRI.* Neuroimage, 2018. **170**: p. 83-94.
38. Liu, T.T., A. Nalci, and M. Falahpour, *The global signal in fMRI: Nuisance or Information?* Neuroimage, 2017. **150**: p. 213-229.
39. Mitra, A., et al., *Lag structure in resting-state fMRI.* Journal of neurophysiology, 2014. **111**(11): p. 2374-2391.
40. Wu, X., et al., *Dynamic changes in brain lateralization correlate with human cognitive performance.* PLoS biology, 2022. **20**(3): p. e3001560.
41. Glasser, M.F., et al., *A multi-modal parcellation of human cerebral cortex.* Nature, 2016. **536**(7615): p. 171-178.
42. Ji, J.L., et al., *Mapping the human brain's cortical-subcortical functional network organization.* Neuroimage, 2019. **185**: p. 35-57.
43. Dawson, S.T., et al., *Characterizing and correcting for the effect of sensor noise in the dynamic mode decomposition.* Experiments in Fluids, 2016. **57**: p. 1-19.
44. Nozari, E., et al., *Macroscopic resting-state brain dynamics are best described by linear models.* Nature biomedical engineering, 2024. **8**(1): p. 68-84.
45. Luenberger, D.G., *Introduction to Dynamic Systems: Theory, Models, and Applications*. 1st ed. 1991: Wiley.
46. Majeed, W., et al., *Spatiotemporal dynamics of low frequency BOLD fluctuations in rats and humans.* Neuroimage, 2011. **54**(2): p. 1140-1150.
47. Cai, W., et al., *Dynamic causal brain circuits during working memory and their functional controllability.* Nature communications, 2021. **12**(1): p. 3314.
48. Menon, V., et al., *Optogenetic stimulation of anterior insular cortex neurons in male rats reveals causal mechanisms underlying suppression of the default mode network by the salience network.* Nature Communications, 2023. **14**(1): p. 866.
49. Fransson, P., *Spontaneous low-frequency BOLD signal fluctuations: An fMRI investigation of the resting-state default mode of brain function hypothesis.* Human brain mapping, 2005. **26**(1): p. 15-29.
50. Gazzaley, A. and A.C. Nobre, *Top-down modulation: bridging selective attention and working memory.* Trends in cognitive sciences, 2012. **16**(2): p. 129-135.
51. Gazzaley, A., et al., *Functional interactions between prefrontal and visual association cortex contribute to top-down modulation of visual processing.* Cerebral cortex, 2007. **17**(suppl_1): p. i125-i135.
52. Chen, X., E. Viding, and T. Nichols, *Faster Accelerated Permutation Inference for the ACE Model (APACE) with Parallelization.* 2017.
53. Schöttner, M., et al., *Exploring the latent structure of behavior using the Human*

Connectome Project's data. Scientific Reports, 2023. **13**(1): p. 713.
54. Barch, D.M., et al., *Function in the human connectome: task-fMRI and individual differences in behavior.* Neuroimage, 2013. **80**: p. 169-189.
55. Cole, M.W., et al., *Intrinsic and task-evoked network architectures of the human brain.* Neuron, 2014. **83**(1): p. 238-251.
56. Vidaurre, D., S.M. Smith, and M.W. Woolrich, *Brain network dynamics are hierarchically organized in time.* Proceedings of the National Academy of Sciences, 2017. **114**(48): p. 12827-12832.
57. Bolt, T., et al., *A parsimonious description of global functional brain organization in three spatiotemporal patterns.* Nature Neuroscience, 2022. **25**(8): p. 1093-1103.
58. Spreng, R.N., et al., *Attenuated anticorrelation between the default and dorsal attention networks with aging: evidence from task and rest.* Neurobiology of aging, 2016. **45**: p. 149-160.
59. Hampson, M., et al., *Functional connectivity between task-positive and task-negative brain areas and its relation to working memory performance.* Magnetic resonance imaging, 2010. **28**(8): p. 1051-1057.
60. Brincat, S.L., et al., *Interhemispheric transfer of working memories.* Neuron, 2021. **109**(6): p. 1055-1066. e4.
61. Ringo, J.L., et al., *Time is of the essence: a conjecture that hemispheric specialization arises from interhemispheric conduction delay.* Cerebral Cortex, 1994. **4**(4): p. 331-343.
62. Ocklenburg, S. and Z.V. Guo, *Cross-hemispheric communication: Insights on lateralized brain functions.* Neuron, 2024.
63. Thompson, G.J., et al., *Short-time windows of correlation between large-scale functional brain networks predict vigilance intraindividually and interindividually.* Human brain mapping, 2013. **34**(12): p. 3280-3298.
64. Moneta, N., et al., *Task state representations in vmPFC mediate relevant and irrelevant value signals and their behavioral influence.* Nature Communications, 2023. **14**(1): p. 3156.
65. O'Doherty, J., et al., *Abstract reward and punishment representations in the human orbitofrontal cortex.* Nature neuroscience, 2001. **4**(1): p. 95-102.
66. Corbetta, M. and G.L. Shulman, *Control of goal-directed and stimulus-driven attention in the brain.* Nature reviews neuroscience, 2002. **3**(3): p. 201-215.
67. Andrews-Hanna, J.R., et al., *Functional-anatomic fractionation of the brain's default network.* Neuron, 2010. **65**(4): p. 550-562.
68. Smith, S.M., et al., *Correspondence of the brain's functional architecture during activation and rest.* Proceedings of the national academy of sciences, 2009. **106**(31): p. 13040-13045.
69. Wang, H., et al., *Evidence of a dissociation pattern in default mode subnetwork functional connectivity in schizophrenia.* Scientific reports, 2015. **5**(1): p. 14655.
70. Li, J., et al., *Topography and behavioral relevance of the global signal in the human brain.* Scientific reports, 2019. **9**(1): p. 14286.
71. Murphy, K., et al., *The impact of global signal regression on resting state correlations: are anti-correlated networks introduced?* Neuroimage, 2009. **44**(3): p. 893-905.
72. Murphy, K. and M.D. Fox, *Towards a consensus regarding global signal regression for resting state functional connectivity MRI.* Neuroimage, 2017. **154**: p. 169-173.
73. Saad, Z.S., et al., *Correcting brain-wide correlation differences in resting-state FMRI.* Brain connectivity, 2013. **3**(4): p. 339-352.
74. Van Essen, D.C., et al., *The WU-Minn human connectome project: an overview.* Neuroimage, 2013. **80**: p. 62-79.

75. Smith, S.M., et al., *Resting-state fMRI in the human connectome project.* Neuroimage, 2013. **80**: p. 144-168.
76. Bianciardi, M., et al., *Sources of functional magnetic resonance imaging signal fluctuations in the human brain at rest: a 7 T study.* Magnetic resonance imaging, 2009. **27**(8): p. 1019-1029.
77. Cordes, D., et al., *Frequencies contributing to functional connectivity in the cerebral cortex in "resting-state" data.* American journal of neuroradiology, 2001. **22**(7): p. 1326-1333.
78. Casorso, J., et al., *Dynamic mode decomposition of resting-state and task fMRI.* NeuroImage, 2019. **194**: p. 42-54.
79. Stoica, P. and R.L. Moses, *Spectral analysis of signals*. Vol. 452. 2005: Pearson Prentice Hall Upper Saddle River, NJ.
80. Biswal, B.B., et al., *Toward discovery science of human brain function.* Proceedings of the national academy of sciences, 2010. **107**(10): p. 4734-4739.
81. Yeo, B.T., et al., *The organization of the human cerebral cortex estimated by intrinsic functional connectivity.* Journal of neurophysiology, 2011.
82. Roll, J., *Local and piecewise affine approaches to system identification*. 2003: Univ.
83. Leonardi, N. and D. Van De Ville, *On spurious and real fluctuations of dynamic functional connectivity during rest.* Neuroimage, 2015. **104**: p. 430-436.
84. Rubinov, M. and O. Sporns, *Complex network measures of brain connectivity: uses and interpretations.* Neuroimage, 2010. **52**(3): p. 1059-1069.
85. Raut, R.V., et al., *On time delay estimation and sampling error in resting-state fMRI.* Neuroimage, 2019. **194**: p. 211-227.
86. Winkler, A.M., et al., *Permutation inference for the general linear model.* Neuroimage, 2014. **92**: p. 381-397.

Figures

Figure 1

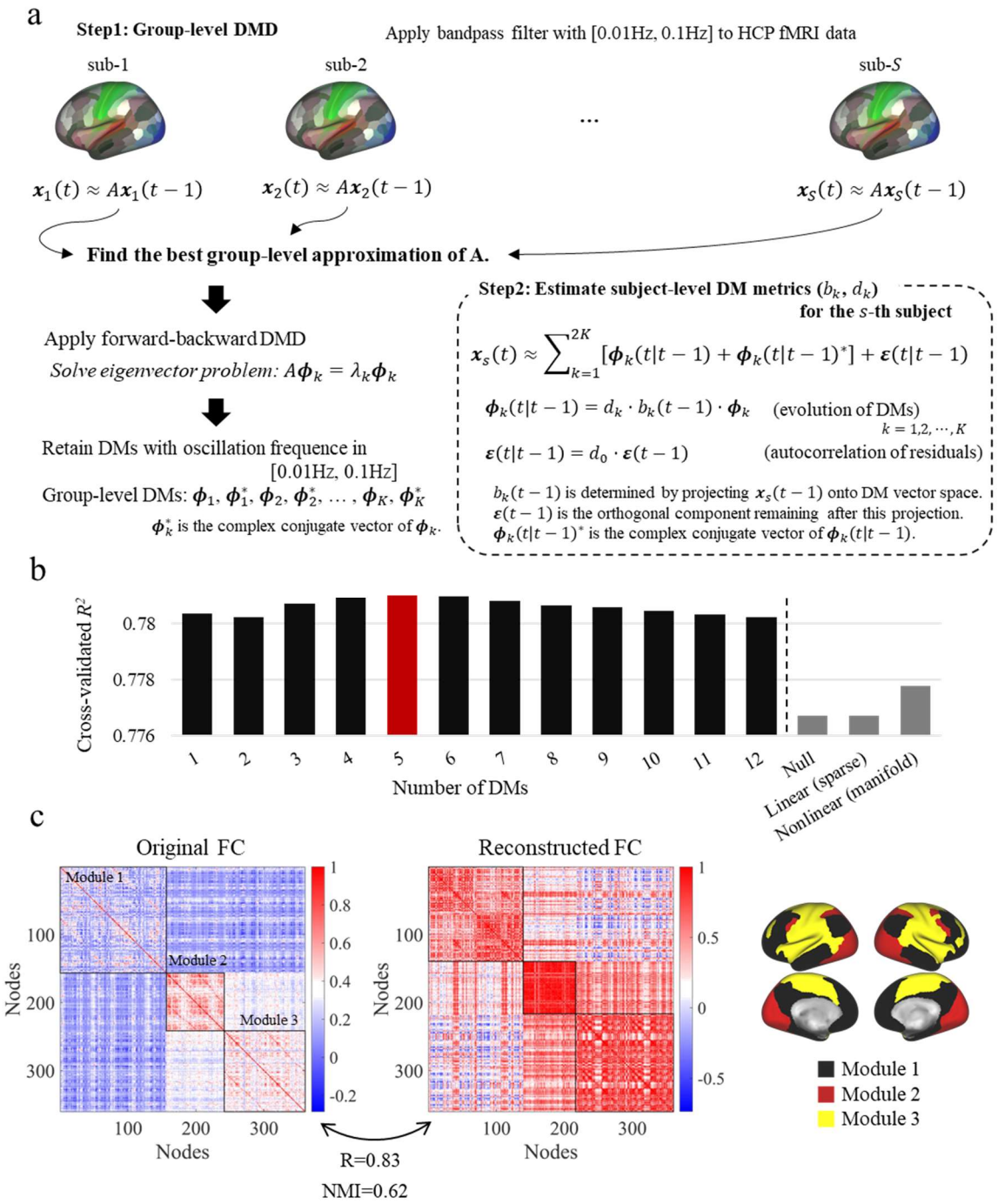

Figure 1. (a) Schematic of group-level Dynamic Mode Decomposition (DMD) applied to resting-state fMRI data and the estimation of subject-specific DM metrics with K DMs: mode-engagement level ($|b_k|$), persistence rate ($|d_k|$),), and progression rate ($\tan^{-1}(\mathrm{Re}(d_k)/$

$\mathrm{Im}(d_k)$)). **(b)** Prediction performance, indicated by cross-validated R^2, using different numbers of DMs, as well as using alternative models (i.e., LASSO and manifold-based model) for comparison. DMs were incrementally included based on the magnitude of their group-level evolution coefficients (λ_k; see Methods), reflecting their contributions to the overall dynamics. Models incorporating DMs consistently outperformed the best previously evaluated models in predicting future BOLD signals [44]. The highest prediction accuracy was achieved using five DMs. **(c)** FC network reconstructed by the five DMs. **Left panel:** FC matrix of cortical BOLD time courses (i.e., original FC matrix). **Middle panel:** Correlation matrix reconstructed from the five DMs. **Right panel:** Module assignments for each ROIs using the cortical FC matrix. Both the original and reconstructed correlation matrices are ordered and outlined according to the modular structure identified by Newman's spectral community detection algorithm, respectively. The community analysis revealed three modules corresponding to the DMN, visual, and SM networks. Although the reconstructed FCs are predominantly positive, the correlation patterns between the original and reconstructed matrices are highly similar (R = 0.83). Additionally, the modular structures of the original and reconstructed matrices show strong similarity (NMI = 0.62), with 87% of ROIs correctly matched.

Figure 2

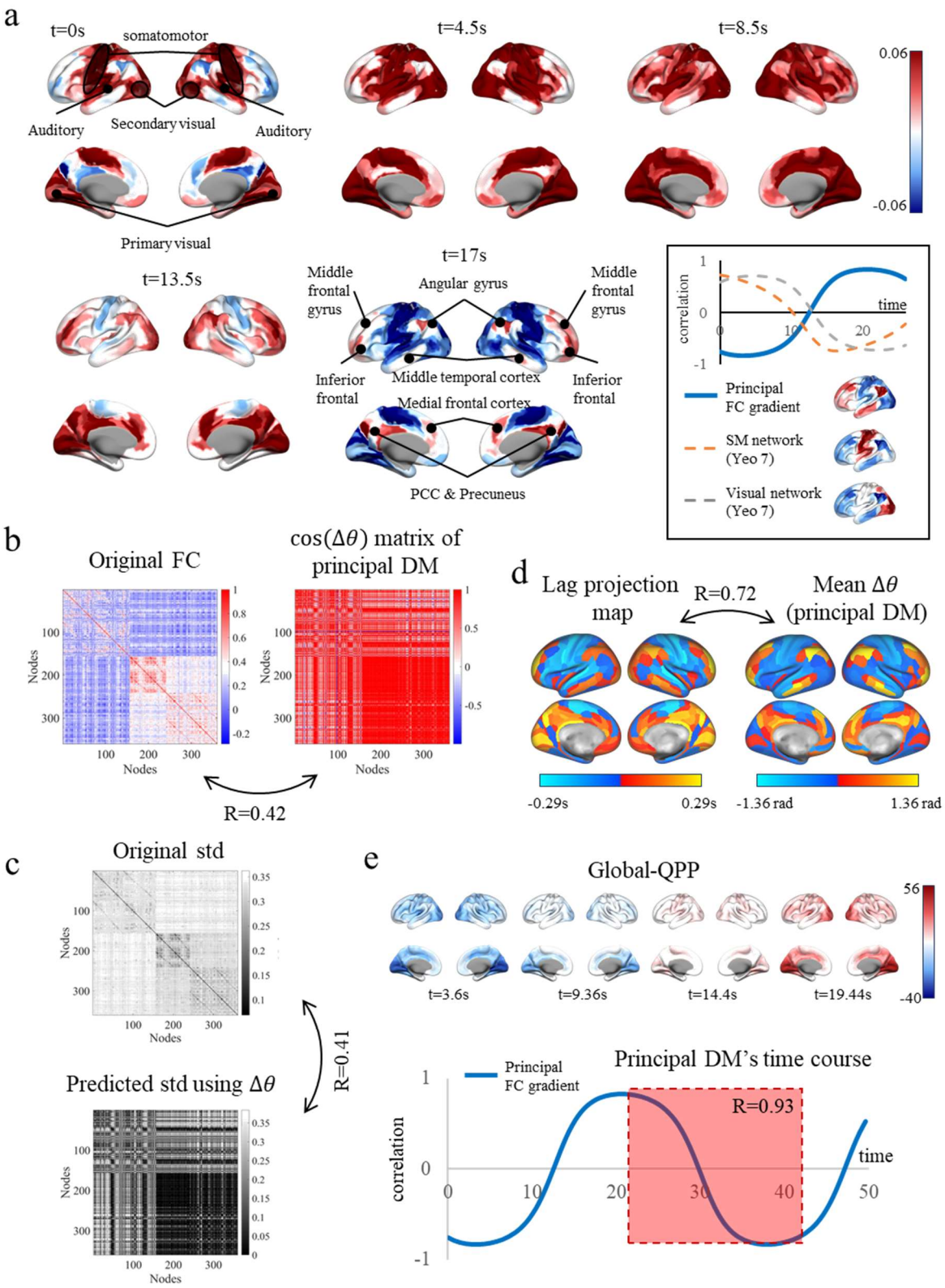

Figure 2. (a) Reconstructed timepoints of the principal DM. In this illustration, unimodal

regions—including the primary visual, secondary visual, auditory, and SM regions—are positively activated at $t = 0$. As time progresses, the signal gradually propagates to transmodal cortical regions that largely overlap with the DMN. This propagation is evidenced by the correlation of spatial pattern at each time point with the principal FC gradient, SM network, and visual network (the latter two networks were obtained from Yeo's 7-network parcellation; see Methods), as shown in the inset. Near the initial time point ($t \approx 0$), the spatial pattern of the principal DM shows a strong correlation with the SM and visual networks ($R > 0.7$) and a negative correlation with the principal FC gradient. Around $t \approx 17.5$, the spatial pattern exhibits a strong correlation with the principal FC gradient ($R > 0.7$). Note that DMs demonstrate periodic evolution. Consequently, the principal DM also reflects transmodal activation propagating back to unimodal regions, indicating bidirectional signal propagation along the unimodal-transmodal axis. Refer to the lower panel of Figure 2e for reconstructed time points over extended durations, summarized by the correlation with the principal FC gradient. **(b) Left panel:** Original FC matrix computed from cortical BOLD time series. **Right panel:** Exact reconstruction of the FC matrix for the principal DM, obtained by calculating the cosine of the phase difference ($\Delta\theta$) between pairs of ROIs. **(c) Upper panel:** Std matrix representing temporal fluctuations of FC in the cortical BOLD time series (i.e., the original std matrix). **Lower panel:** Reconstruction of the standard deviation matrix of temporal FC fluctuations using the phase differences between pairs of ROIs in the principal DM. Even using this single DM, the reconstructed FC and std matrices show moderate correlations with the original matrices ($R = 0.41$ and $R = 0.39$, respectively). **(d) Left panel:** Lag projection map derived from cortical BOLD time series, illustrating the average time delay (in seconds) for each cortical ROI. **Right panel:** Average phase difference map of the principal DM, showing the average phase lag (in radians) for each cortical ROI. The strong correlation between the lag projection and average phase difference maps ($R = 0.72$) indicates that the time delays in the

BOLD signal are predominantly influenced by the principal DM. **(e) Upper panel:** Spatiotemporal pattern observed in the global QPP (i.e., QPP obtained without GSR). The global QPP exhibits a widespread pattern of activity with positive correlations across brain regions. **Lower panel:** Reconstructed time points of the principal DM, summarized by the correlation with the principal FC gradient at each time point. The global QPP showed a strong correlation with interval when the principal DM displays a decrease in correlation with the principal FC gradient (R = 0.93), indicating that the global QPP largely reflects the temporal evolution of the principal DM.

Figure 3

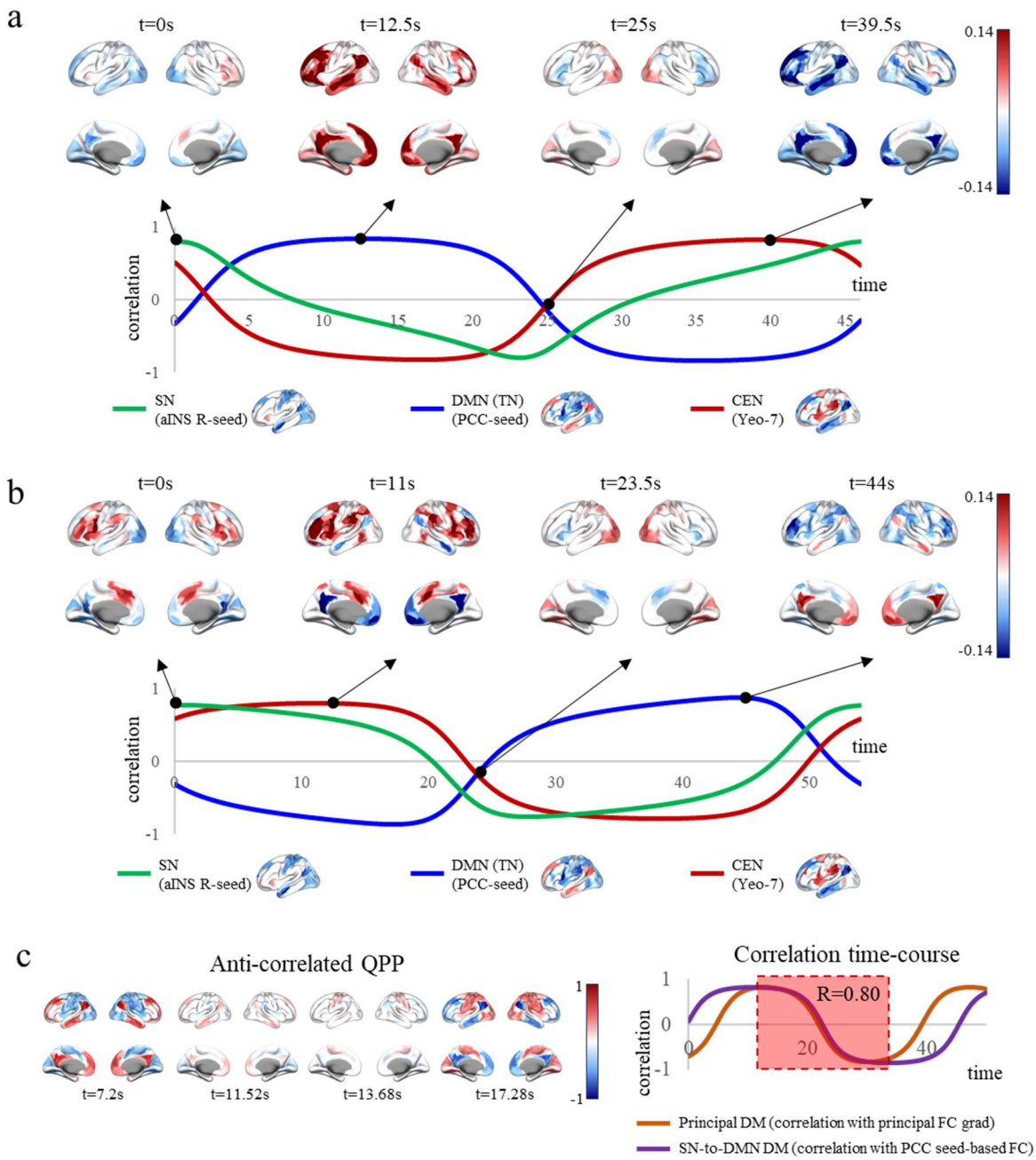

Figure 3. DMs 2 and 3. Reconstructed timepoints of **(a)** SN-to-DMN DM and **(b)** SN-to-CEN DM, along with the correlation time-courses between spatial patterns at each time point and the SN, DMN, and CEN. The spatial topography of SN is derived from right anterior insula (aINS R) seed-basedFC (Supplementary Figure 9a). The spatial topography of DMN is derived from PCC seed-based FC (Supplementary Figure 9b). CEN is obtained from the Yeo's 7

network partition (Supplemenatry Figure 5c). These two DMs represent distinct transitions from SN activation: one transitions to the DMN and the other to the CEN. Both DMs exhibit anti-correlated patterns between the DMN and CEN: In the SN-to-DMN DM, DMN activation transitions to CEN; in constrast, in the SN-to-CEN DM, CEN activation transitions to DMN. **(c) Left Panel:** Spatiotemporal pattern of the anti-correlated QPP (i.e., QPP obtained with GSR). This QPP shows opposing activity between DMN (TN) and CEN (TP) regions. **Right Panel:** Correlation time-course of the principal DM and the SN-to-DMN DM. The principal DM's time course is represented by the correlation with the principal FC gradient at each time point, while the SN-to-DMN DM represented by the correlation with the DMN (PCC seed-based FC). The combined spatiotemporal pattern of these two DMs (during both decreasing activity in transmodal regions and the DMN) highly correlates with the spatiotemporal pattern of the anti-correlated QPP (R = 0.80).

Figure 4

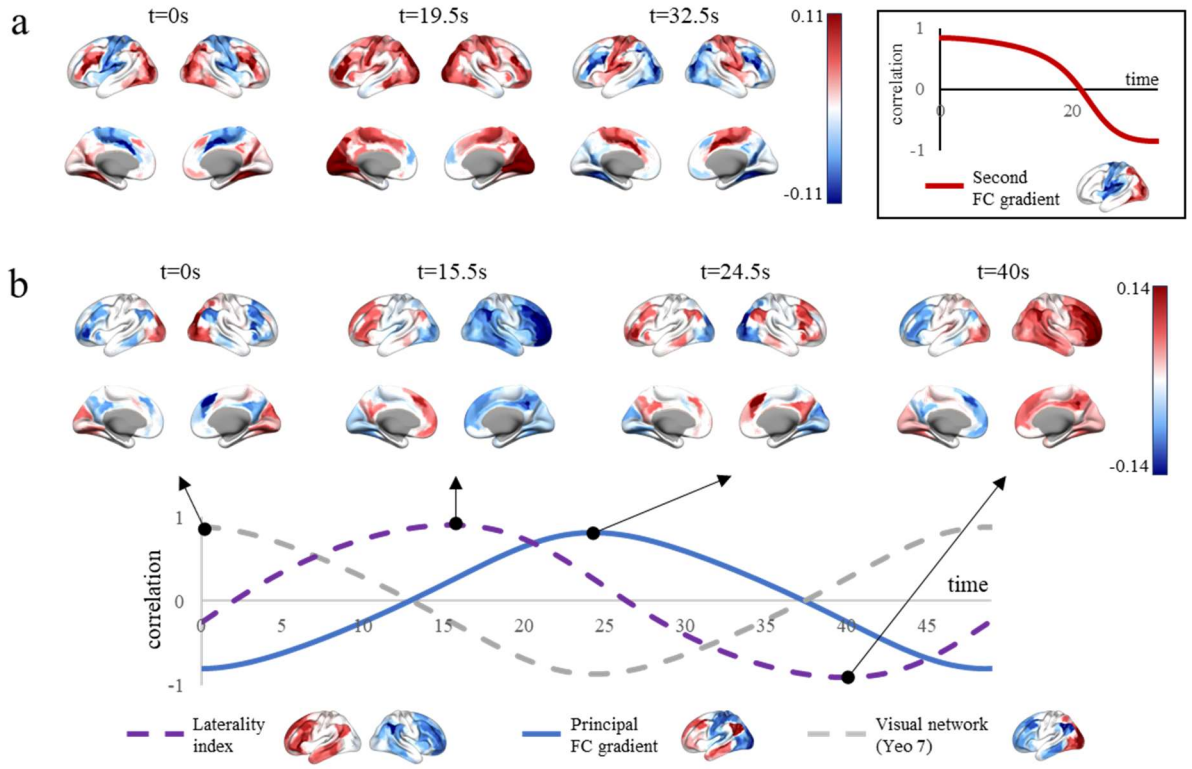

Figure 4. DMs 4 and 5. **(a)** Reconstructed timepoints of the FV-to-SM DM, along with the correlation time-courses between spatial patterns at each time point and the second FC gradient. This correlation indicates that signals within this DM propagate along the visual-SM axis. The synchronized activity between frontal regions and visual areas suggests that frontal regions may play a role in coordinating motor responses derived from sensory inputs. **(b)** Reconstructed time points of the bi-asym DM, along with the correlation time courses between spatial patterns at each time point and the LI, principal FC gradient, and visual network (from Yeo's 7-network partition). In this DM, activation progresses from visual regions to left DMN regions and subsequently transitions to right DMN regions. The spatial activity patterns of the lateralization in this DM is highly correlated with the LI (R = ±0.91), indicating that this DM effectively reflects dominant hemispheric lateralization in brain dynamics. The positive correlation with the LI indicates left hemispheric dominance in activation; meanwhile, the negative correlation indicates right hemispheric dominance. The presence of this lateralized

DM underscores the significance of hemispheric lateralization in brain function.

Figure 5

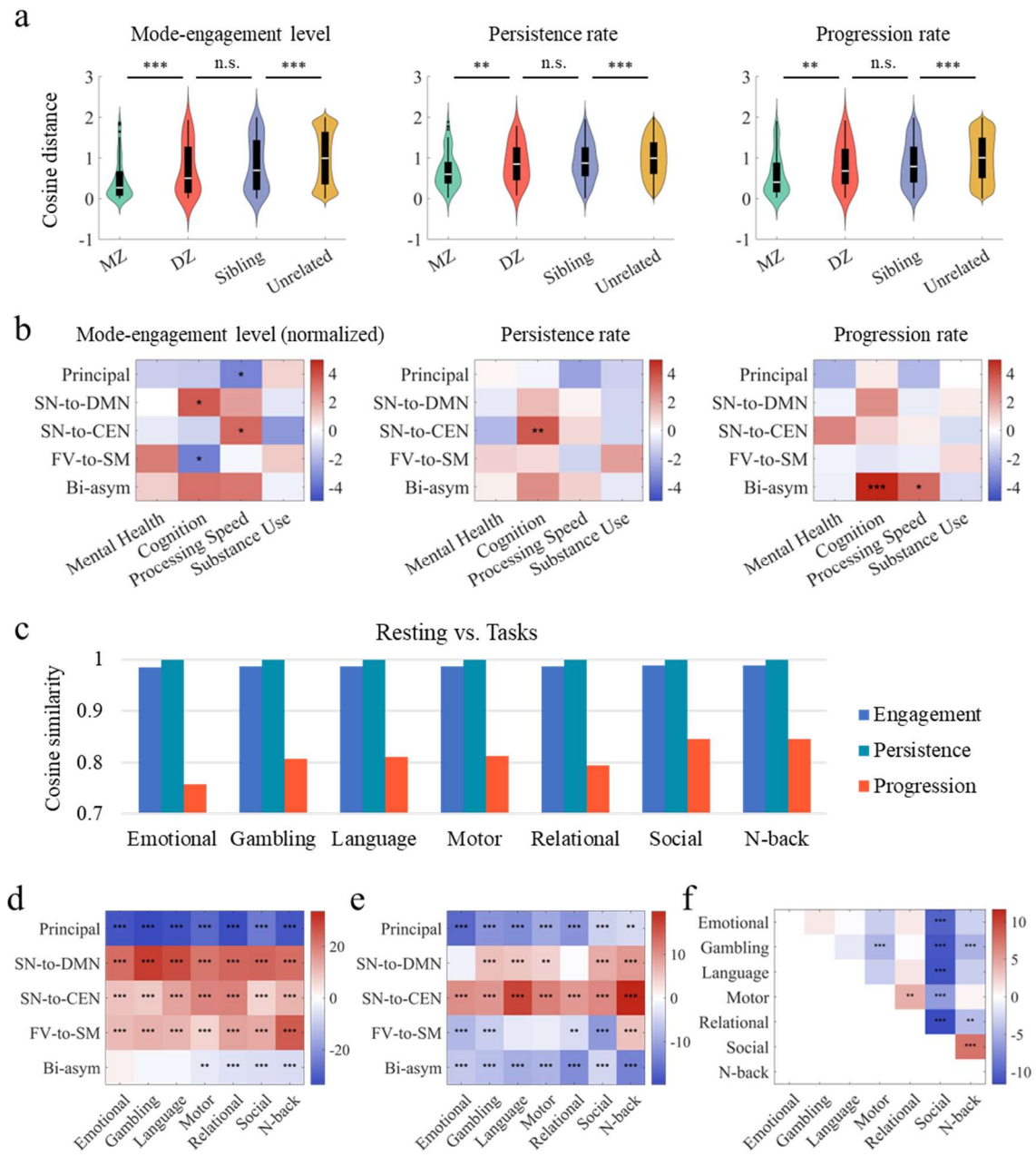

Figure 5. Influences of genetics, behavior, and task. **(a)** Cosine distances between DM metrics for each pair of MZ twins, DZ twins, siblings, and unrelated individuals. Distances were calculated separately for mode-engagement levels, persistence rates, and progression rates due to differences in value ranges and distributions. The plotted distances represent residuals after regressing out confounding variables (e.g., age, gender, years of education, and others; see Methods). **(b)** T-value heatmap illustrating the correlation between four behavioral latent

factors—mental health, cognition, processing speed, and substance use—and the DM metrics. P-values were FWE-corrected (family-wise error corrected) for all 60 tests (combinations of three DM metrics, five DMs, and four behavioral factors) via permutation methods (see Methods). Mode-engagement levels were normalized so that the sum of the five values for each subject equals 1, facilitating the assessment of each DM's engagement ratio (referred to as normalized mode-engagement level). See Supplementary Tables 1-6 for the detailed statistical results. **(c)** Similarity of DM metrics between resting and task states. Similarities were evaluated separately for mode-engagement levels, persistence rates, and progression rates due to differences in value ranges and distributions. All three metric types exhibited high similarity between resting and task states (CS > 0.7). **(d–f)** T-value heatmaps comparing DM metrics between resting and task states: **(d)** Normalized mode-engagement rates in resting versus task states, **(e)** Progression rates in resting versus task states, and **(f)** Normalized mode-engagement rates of the principal DM across all pairs of seven tasks. In comparisons between resting and task states, positive t-values (red) indicate higher DM metrics during tasks (labeled on the column) compared to rest, while negative t-values (blue) indicate lower metrics during tasks. In comparisons among task states, positive t-values (red) signify that the DM metric for the task labeled on the row is significantly greater than that for the task labeled on the column, and negative t-values (blue) indicate the opposite. P-values for resting vs. task comparisons were Bonferroni-corrected separately for the three DM metric types. For task state comparisons, p-values were Bonferroni-corrected across all five DMs and all possible pairs of the seven tasks (resulting in $5 \times \binom{7}{2} = 105$ comparisons), while still correcting separately for the three types of DM metrics. See Supplementary Figures 11–14 for additional comparison results. Asterisks indicate statistical significance (*p < 0.05, **p < 0.01, ***p < 0.001).